IN-33-CR
111321
101 P.

JPL Publication 87-29

Interferometry Theory for the Block II Processor

J. B. Thomas

(NASA-CR-181551) INTERFEROMETRY THEORY FOR THE BLOCK 2 PROCESSOR (Jet Propulsion Lab.) 101 p CSCL 09C

N88-12730

Unclas
G3/33 0111321

October 15, 1987

National Aeronautics and Space Administration

Jet Propulsion Laboratory
California Institute of Technology
Pasadena, California

JPL Publication 87-29

Interferometry Theory for the Block II Processor

J. B. Thomas

October 15, 1987

NASA

National Aeronautics and
Space Administration

Jet Propulsion Laboratory
California Institute of Technology
Pasadena, California

The research described in this publication was carried out by the Jet Propulsion Laboratory, California Institute of Technology, under a contract with the National Aeronautics and Space Administration.

ABSTRACT

This report presents interferometry theory for the Block II processor, including a high-level functional description and a discussion of data structure. The analysis covers the major processing steps: cross-correlation, fringe counter-rotation, transformation to the frequency domain, phase calibration, bandwidth synthesis, and extraction of the observables of amplitude, phase, phase rate, and delay. Also included are analyses for fractional bitshift correction, station clock error, ionosphere correction, and effective frequencies for the observables.

ACKNOWLEDGMENTS

I am grateful to Bob Treuhaft, Steve Unwin, Marty Ewing, Roger Linfield, Chad Edwards, Tom Lockhart, and Elliot Sigman for their helpful suggestions after reading a draft of this report.

CONTENTS

Figures

Table

DEFINITIONS OF SYMBOLS

a_1	=	first harmonic of quantized stopping function
$A(\hat{k},\omega)$	=	random Fourier amplitude at frequency ω received from direction $\hat{k}$ for an extended source
A_s	=	estimated amplitude in fringe fitting
$A(\omega)$	=	random Fourier amplitude at frequency ω for a point source
b	=	bit interval, typically 250 nsec
$\vec{B}_r$	=	retarded baseline
c	=	speed of light
c_k	=	relative fringe amplitude, bin k
c_{mk}	=	model for relative fringe amplitude, bin k
D_A	=	$D_N/(2\ W)$
D_N	=	amplitude normalization
d_s	=	source diameter
d(t)	=	normalized noise added to calibration signal
$d\Omega$	=	differential solid angle
$E(\vec{x}, t)$	=	electric field at $\vec{x}$, t
F_q	=	quantization or fractional bitshift filter
$\overline{G^2}$	=	average of square of bandpass amplitude across W
$G_j(\omega)$	=	bandpass amplitude at station j
$h(\omega_k,t_G)$	=	initial frequency-domain fringes
$h'(\omega_k,t_G)$	=	frequency-domain fringes after fractional bit-shift correction
$h''(\omega_k,t_G)$	=	frequency-domain fringes after phase calibration
$h_c(\omega_k,t_G)$	=	frequency-domain fringes after amplitude normalization

$\hat{k}$ = apparent wave vector

$\hat{k}_a$ = apparent wave vector from reference point in source

k_e = proportionality constant in ionosphere phase

$\hat{k}_m$ = model for direction of source wave vector

ℓ = lag offset of correlator

N_c = number of BWS channels

n_k = normalized additive noise, station k

N_t = number of bits in fringe-stopping sum

q_k = normalized natural source signal, station k

$R_B(u,v)$ = brightness transform

r_m = "calibrated" fringe amplitude

$R_m(\tau_f,\omega_f)$ = model fringes in BWS-delay/fringe-frequency domain

$r(t_G,\ell)$ = cross-correlation function

$R(\tau_f,\omega_f)$ = $R'(\tau_f,\omega_f)$ corrected for FFT origin offsets

$R'(\tau_f,\omega_f)$ = initial fringes in BWS-delay/fringe-frequency domain

S_c = correlated flux

S_F = total source flux

$S_p(\omega)$ = natural source power spectrum

$S_T(\Delta\omega)$ = frequency resolution function resulting from FFT over lag

t = true time

t_1 = value of t_G for first point

$\hat{t}_{bj}$ = shorthand for arguments in Eq. 6.7

t_{bk} = bit time, station k

T_c = correlation interval of 25 msec (10^5 bits)

t_{ck} = ϕ-cal time, station k

t_G = common Greenwich time

t''_G = $t_G - t_1$

T_M = maximum integration time

T_n = additive noise temperature

t_o = true time "origin"

t_{pk} = true time that corresponds to bit time t_{bk}, station k

T_q = natural-source noise temperature

T_s = total or system noise temperature

t_s = correlator reference time

t_z = reference time in fringe-fitting

u = component of sky-projected baseline vector in direction of right ascension in units of wavelength

$u_\ell(t_G)$ = complex stopped fringes for lag ℓ at time t_G

v = component of sky-projected baseline vector in direction of declination in units of wavelength

v_f = fringe visibility = correlated flux/total flux

V_k = baseband voltage signal, station k

W = nominal recording bandwidth = sample rate/2 = 2 MHz

$\vec{x}$ = position vector in geocentric coordinates

$\vec{x}_k(t)$ = location of station k as function of true time

$\vec{x}_{mk}$ = model for position of station k

y_k = doppler-shifted frequency, station k

z_k = normalized analog signal at station k

α = right ascension

α_{IK} = composite effect of instrumental phase shifts, station k

β = structure coordinate in direction of right ascension

γ = structure coordinate in direction of declination

Δf_s = spanned bandwidth

Δ_k = fixed integer-bit delay introduced by correlator

ΔN_e = differential electron content through ionosphere, station j minus station i

$\Delta\tau_c$ = residual clock offset

$\Delta\tau_{cs}$ = correction required to remove effects of clock errors

$\Delta\tau_g$ = residual geometric delay

$\Delta\tau_R$ = residual delay in calibrated fringes

$\Delta\tau_R'$ = residual delay in uncalibrated fringes

$\Delta\tau_t$ = residual troposphere delay

$\Delta\dot{\tau}_\phi$ = maximum residual phase delay rate

$\Delta\phi_f$ = stopped fringe phase

$\Delta\phi_h$ = "stopped heterodyne phase," station k*

$\Delta\phi_k^T(\omega_n)$ = stopped phase of n^{th} tone, station k

$\Delta\omega_c$ = true frequency minus nominal frequency

δ = declination of source

ε_A = fractional decrease in fringe amplitude

ε_k = tweak frequency to remove effect of lag offsetting

η_k = all noise added to recorded signal, station k

θ_k = baseband signal phase at station k

θ_q = phase of quantization filter, F_q

κ_k = antenna sensitivity at station k

λ = wavelength of recorded radio signal

τ_{ak} = antenna delay* before injection point, station k

τ_{bk} = error in bit time*, station k

---

*Use without subscript denotes difference j minus i

τ_{BWS} = final BWS delay

τ_{ck} = error in ϕ-cal time*, station k

τ_{ck}^{m} = model clock "delay," station k

τ_{dk} = geometric and troposphere delay for station k

τ_e = group delay due to charged particles

τ_f = BWS "search" parameter in FFT

τ_g = conventional geometric delay

$\tau_{g_{mk}}$ = model geometric delay removed, station k

τ_{Ik} = instrumental group delay*, station k

τ_m = $\tau_{mi} - \tau_{mj}$

τ_{MA} = total model delay to be restored

τ_{mg} = model geometric delay restored

τ_{mk} = retarded correlator model delay, station k

τ_{mk}^{u} = unretarded model delay, station k

τ_s = estimated residual delay from fringe fitting

τ_{tk} = troposphere delay for station k

τ_{tk}^{m} = model troposphere delay, station k

τ_{uk} = delay between clock reference point and ϕ-cal injection point, station k

τ_x = interim geometric delay

τ_ϕ = final phase delay

$\dot{\tau}_{\phi s}$ = estimated phase-delay rate in fringe fitting

ϕ_B = phase shift due to source structure

ϕ_c = oscillator phase at clock reference point

ϕ_e = phase shift due to charged particles

ϕ_f = total fringe phase before counter-rotation

*Use without subscript denotes difference j minus i

ϕ_h = total heterodyne phase shift

ϕ_{hk} = heterodyne phase shift, station k

ϕ_{IK} = instrumental phase shift*, station k

$\phi_m(t_G)$ = model phase for counter-rotation

ϕ_n = phase of n^{th} ϕ-cal tone at injection point

ϕ_s = estimated phase in fringe fitting

$\phi^T(\omega_k)$ = calibration phase at frequency ω_k

$\psi_c(\omega_k, t_G)$ = corrected fringe phase

ψ_f = residual fringe phase after counter-rotation

ψ^T_{nk} = stopping phase for n^{th} tone, station k

ω = RF frequency in geocentric coordinates

$\hat{\bar{\omega}}$ = estimated "center" frequency of 2-MHz passband used in fringe-counter-rotation

ω_1 = RF frequency of first frequency bin

ω_c = nominal oscillator frequency

ω_f = fringe frequency "search" parameter in FFT

ω_{hk} = true total heterodyne frequency, station k

$\hat{\omega}_{hk}$ = estimated value for ω_{hk}

ω_k = RF frequency for k^{th} bin

ω_k' = $\omega_k - \omega_{hi}$ = baseband value for frequency ω_k

ω_k'' = $\omega_k - \omega_1$

ω^T_n = frequency of n^{th} ϕ-cal tone

ω_t = true oscillator frequency

ω_z = reference frequency in fringe fitting

ω_τ = effective frequency for BWS delay

$\omega_{\dot{\tau}}$ = effective frequency for delay-rate observable

$\omega_{\tau\phi}$ = effective frequency for phase-delay observable

ω_ϕ = effective frequency for phase observable

SECTION I

INTRODUCTION

Over the last few years, a very long baseline interferometry (VLBI) processor, the BLOCK II (BLKII) processor, has been under development at JPL and the California Institute of Technology. The major subsystems and their principal contributors are correlator software (D.H. Rogstad and H.W. Hammond), correlator hardware (J.C. Peterson, B. Rayher, J.W. Dillon, B. Espinoza, and E. H. Sigman), Tensor (M.S. Ewing and J.L. Vavrus), and post-Tensor software (T.G. Lockhart).

Reading each tape channel at a rate as high as 4 Mbits/sec, the current version of the BLKII processor can simultaneously reduce tapes recorded at four stations, including cross-correlation of 28 tape channels for all six station pairs. A single pass through the BLKII processor can reduce many gigabits of data to only four output observables: bandwidth-synthesis (BWS) delay, phase delay, phase-delay rate, and fringe amplitude, with each corrected for instrumental and processing effects.

This report outlines the functional design of the BLKII processor and augments a previous analysis [1] of the BLKO system to obtain a mathematical description of data reduction in the new processor. Even though the theory of data reduction in the BLKII processor is very similar to the BLKO analysis through the step of phase calibration, this report will reproduce much of the analysis and discussion in that report for completeness. As in the BLKO analysis, only nonrelativistic theory will be considered.

The analysis includes all signal processing steps, beginning with the free-space form of the incoming radio wave and tracing its evolution through the station instrumentation, cross-correlation, fringe counter-rotation, transformation from the lag domain to the frequency (RF) domain, phase calibration, fractional-bit-shift correction, coherent integration over time and frequency, observable estimation and model restoration. In addition to system improvements, some of the new features in the analysis include: a new fringe model for least-square estimation of the four output observables (Section XIV); a demonstration of the approximate equivalence of this fringe-fitting procedure to an implicit phase-fitting procedure (Appendix C); formulas for calculating an optimal reference time and reference frequency (Appendix C); a method for calculating effective frequencies to be used in dual-band calibration of charged-particle effects (Appendix E); and a method for correcting the final observables for absolute clock error at each station (Section XII).

SECTION II

SUMMARY OF THE BLOCK II SYSTEM

The primary features of the BLKII processor from input bits to output observables are shown in Figures 1 to 5. Figure 1 shows the major steps in the BLKII processor; Figure 2 defines the indexing convention for station pairs; Figure 3 describes in more detail the processing of a pair of stations through the step of fringe counter-rotation; Figure 4 illustrates with bit-stream manipulations the steps shown in Figure 3, but for a single lag; and Figure 5 illustrates the structure of the data in the steps from cross-correlation to output observables of BWS delay and delay rate.

Data acquisition for the BLKII processor is handled primarily by the Mark III (MKIII) data acquisition system [2], which can simultaneously and continuously record as many as 28 channels on 1-inch instrumentation tape. In its most versatile form, the MKIII system can record each channel at any one of seven rates (0.125, 0.25, 0.5, 1, 2, 4, or 8 Mbits/sec). Present systems, however, are typically configured so they can record each channel at only one rate, 4 Mbits/sec. The Mark III system down-converts channels in upper-sideband/lower-sideband pairs, which leaves 14 channel-pairs that can be arbitrarily divided between bands (e.g., S band and X band). Although the Mark III system is the primary system for the BLKII processor, Mark II tapes can also be processed.

Even though the BLKII processor can accommodate a number of the potential record rates of the MKIII system, this report will assume that the nominal channel bandwidth is 2 MHz and the record rate is 4 Mbits/sec. Results for other record rates can be obtained by scaling according to record rate wherever necessary. Reading each channel at 4 Mbits/sec, the BLKII processor can simultaneously process tapes from as many as four stations, which are combined in pairs to form as many as six baselines. As illustrated in Figures 3 and 4, the bitstream from each station is offset by an a priori delay computed as the difference in time of arrival of the incoming radio signal at the station and at the center of mass of the earth. For geophysical applications, eight lag offsets relative to the a priori delay model are applied to one of the two bitstreams on each baseline. (The spectral line option is considered below.) After multiplication of the multiply-offset bitstreams of a given station pair, the product for each lag is counter-rotated in quadrature to remove rapid phase variations and the result is summed over 25 msec (0.1 Mbits). The resulting complex fringes for each channel are then transformed by a discrete Fourier transform (DFT) over lag to the (RF) frequency domain where, for an 8-lag transform, each 2-MHz channel is sampled at the center of each of four bins of

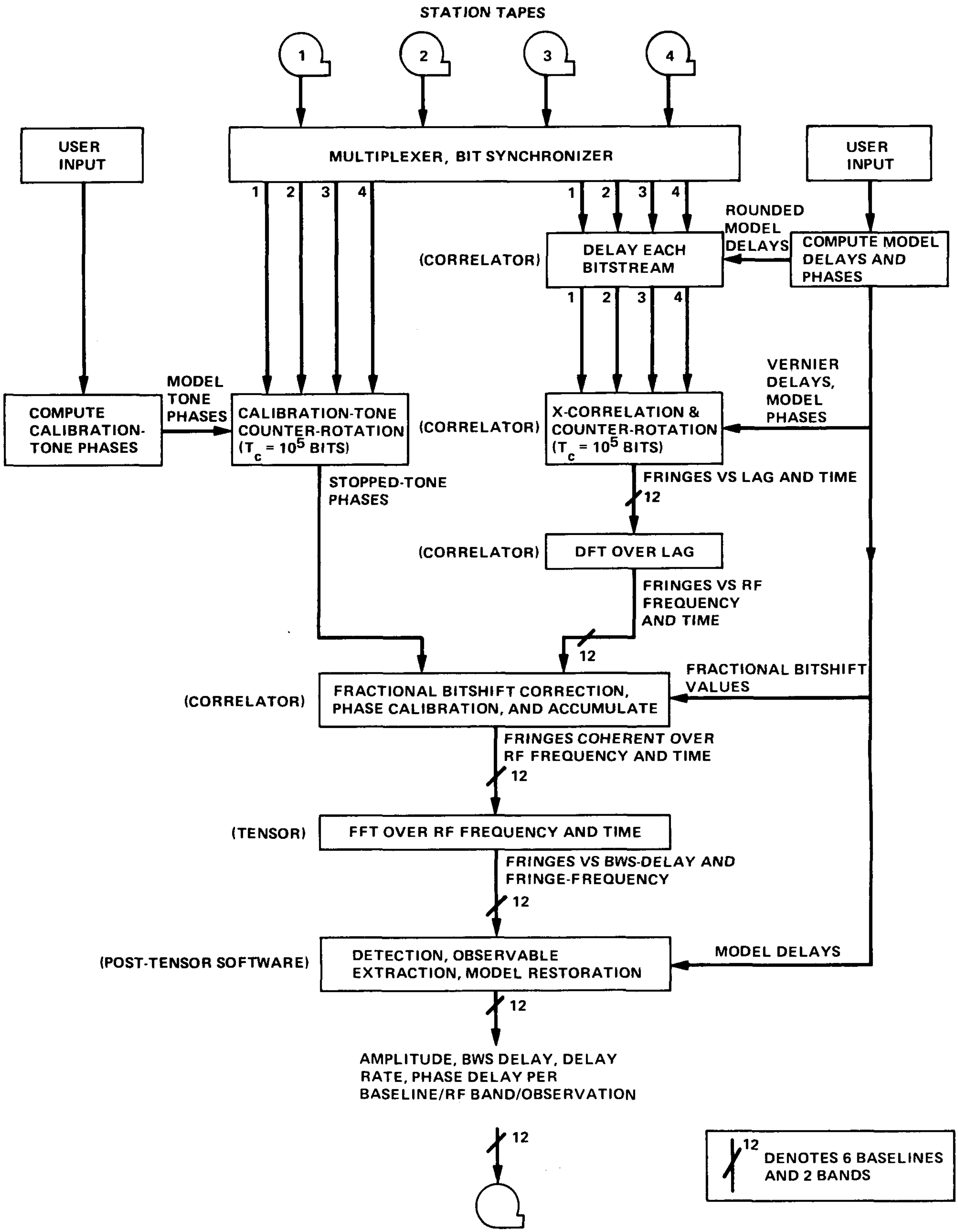

Figure 1. Functional Block Diagram for the Block II Processor

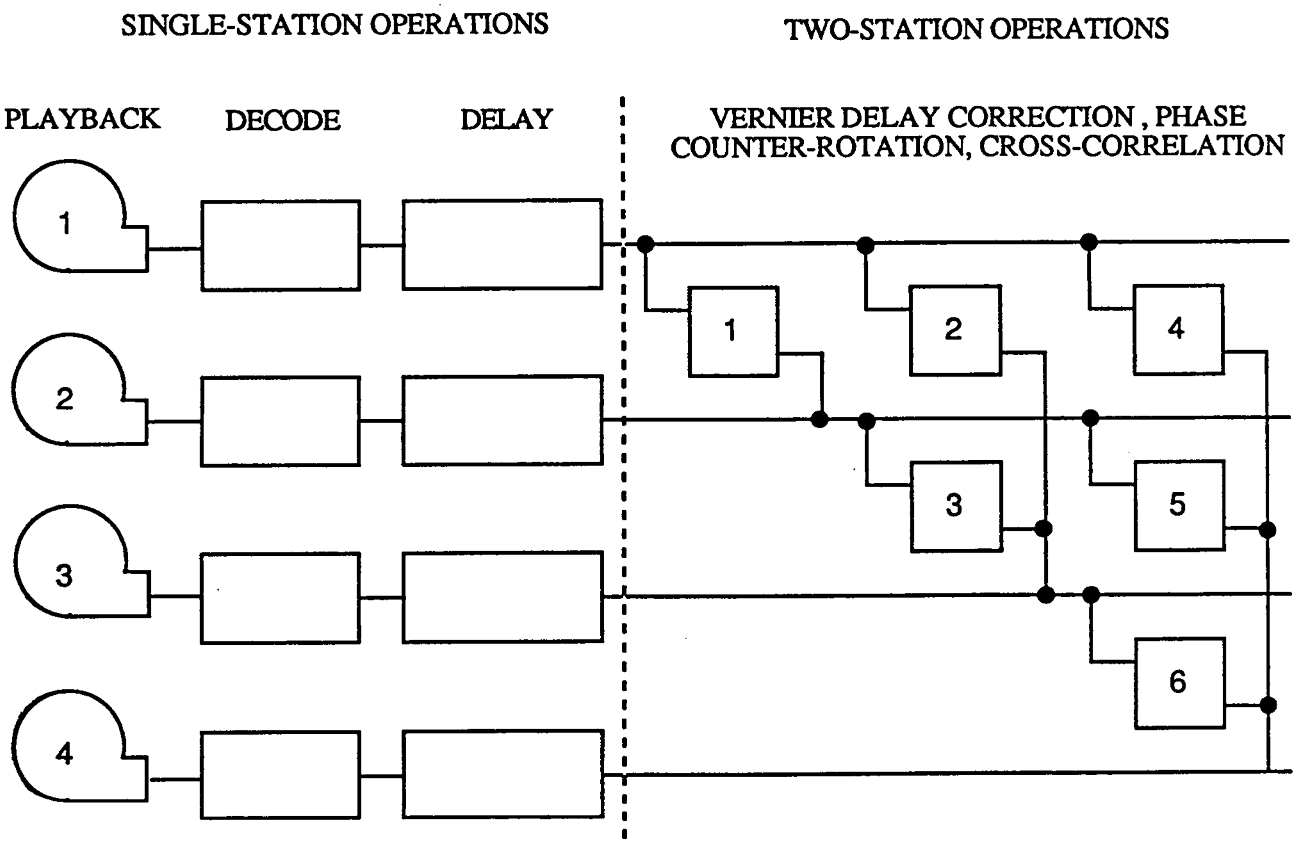

Figure 2. Indexing Convention in the Block II Processor

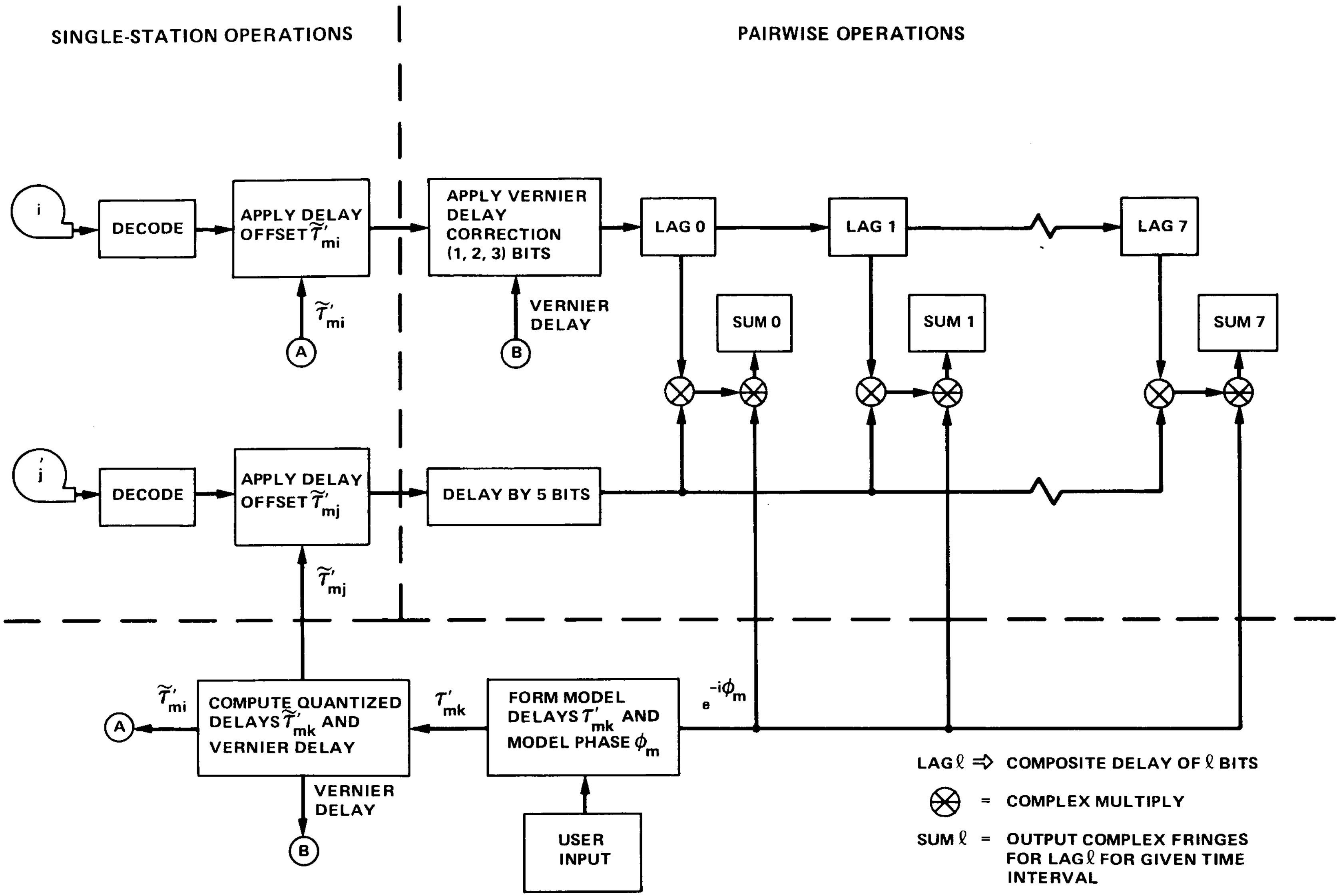

Figure 3. Functional Block Diagram for Two-Station Cross-Correlation in the Block II Processor

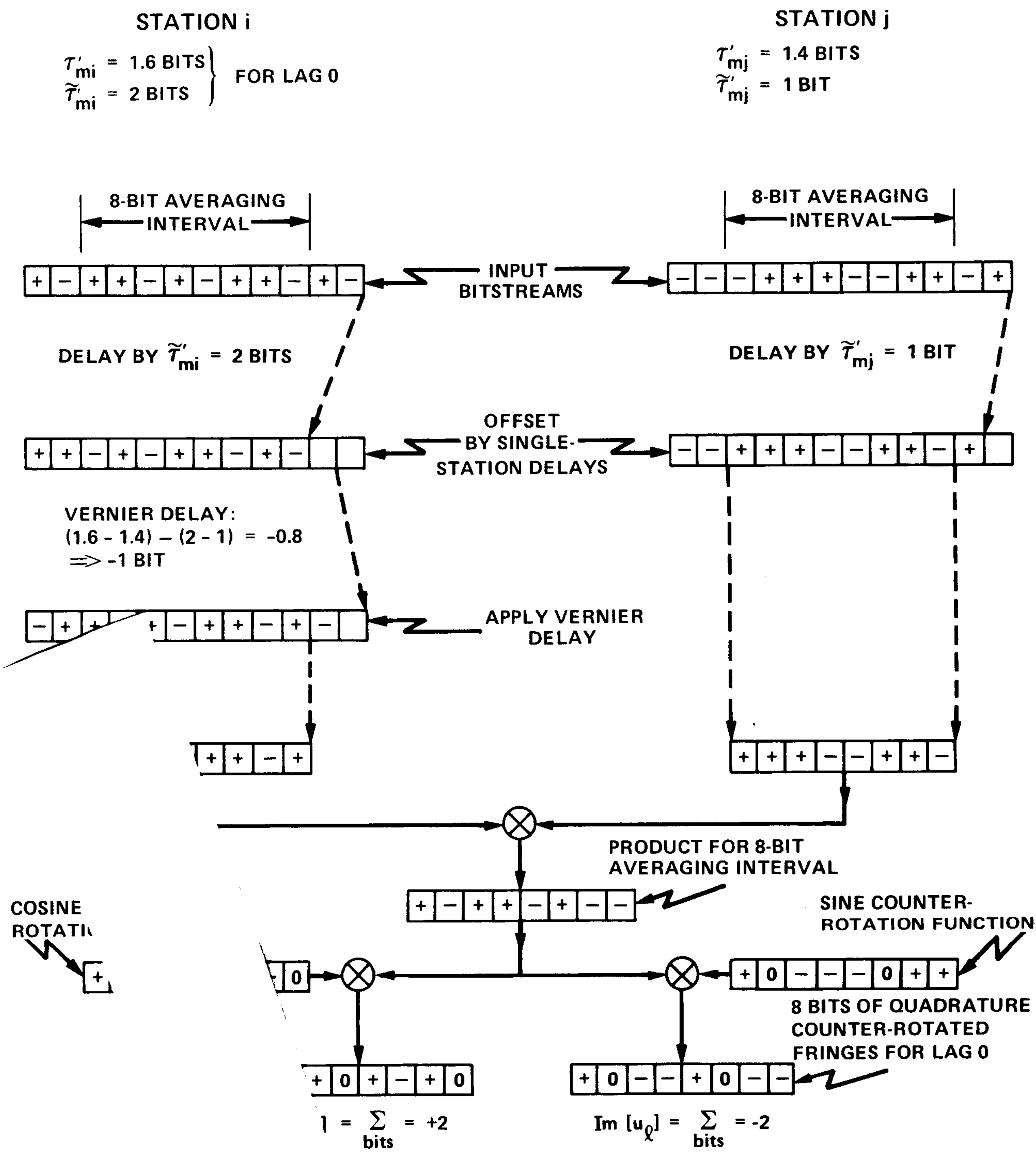

Figure ... fied Illustration of Bit Manipulations in
'I Cross-Correlation. This simplified
ation shows only 8-bit averaging, lag 0,
nally small delays, and abnormally high
tes. It neglects fixed correlator

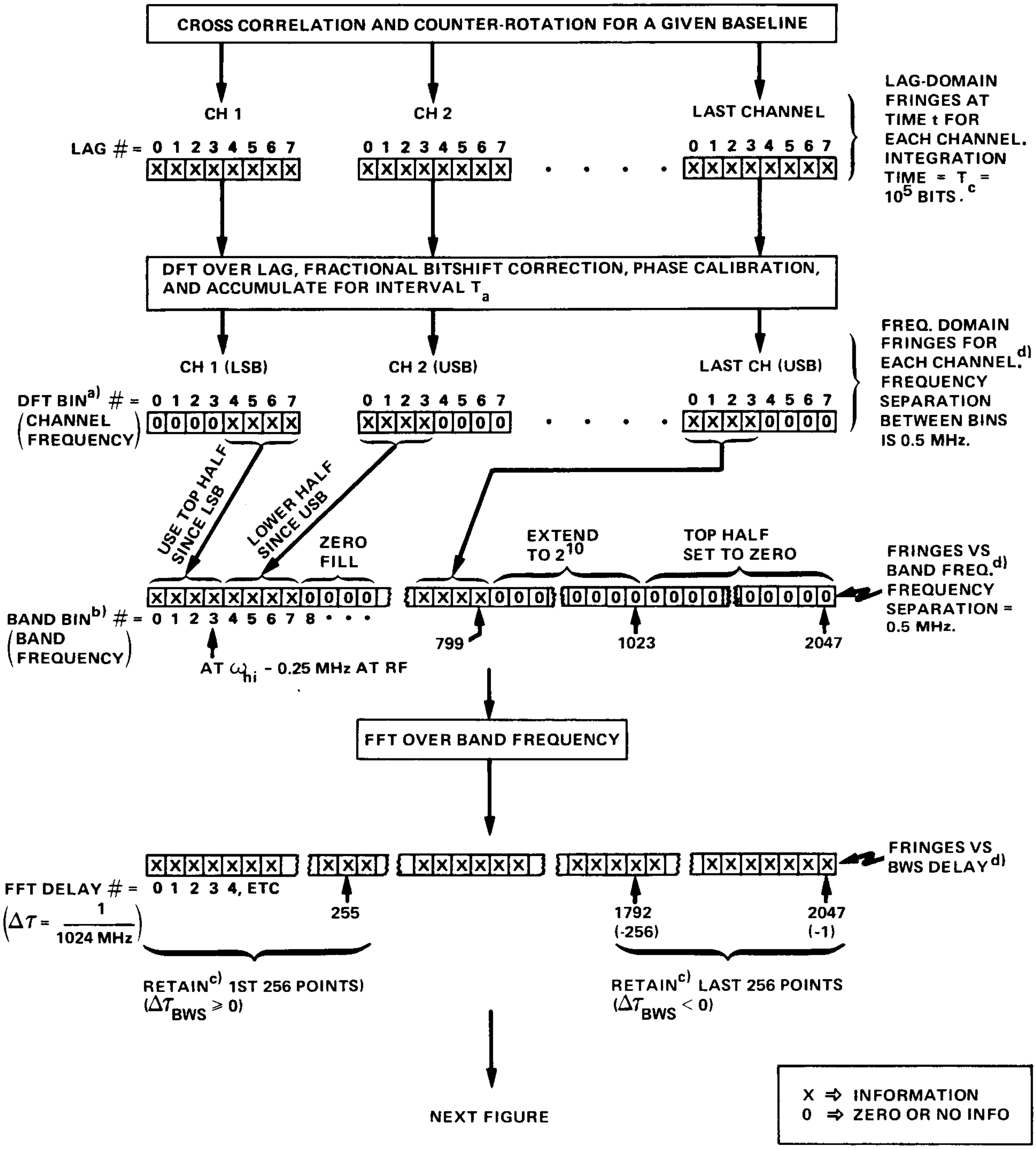

a) EACH BIN IS RELATIVE TO TOTAL HETERODYNE FREQUENCY FOR THE CHANNEL.

b) ASSUMES CHANNEL 0 HAS LOWEST RF FREQUENCY AND THAT TOTAL HETERODYNE FREQUENCIES HAVE BEEN SET WITH SPACING EQUAL TO INTEGER *0.5 MHz.

c) ASSUMES A PRIORI WILL RESTRICT FRINGE SEARCH TO 512 POINTS IN BWS DELAY.

d) TIME TAG AT CENTER OF INTERVAL T_a.

Figure 5a. Schematic Illustration of Data Structure in the Block II Processor: Part I. This illustration is for one source on one baseline over interval T_a and assumes a spanned bandwidth of 400 MHz.

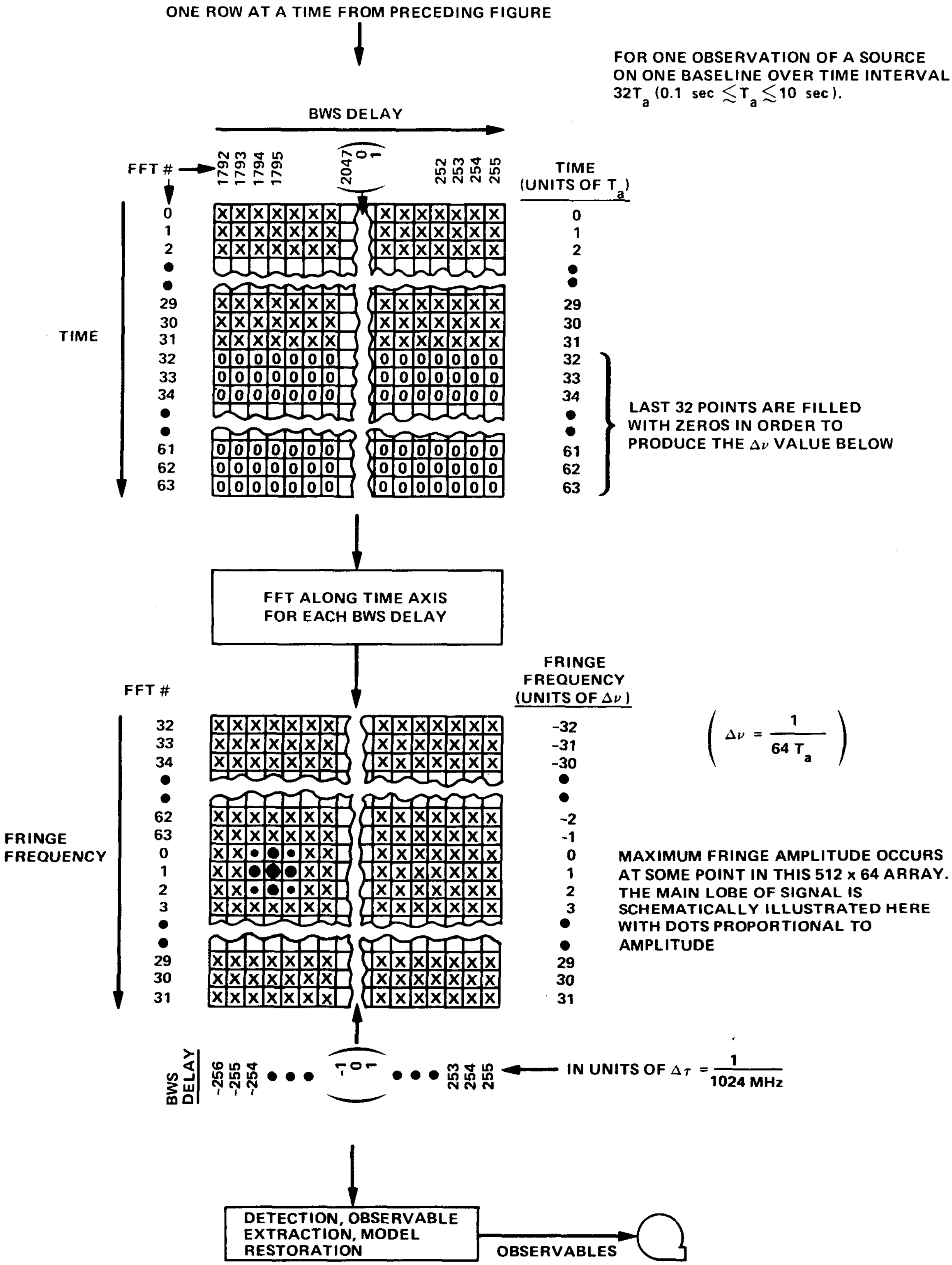

Figure 5b. Schematic Illustration of Data Structure in the Block II Processor: Part II

0.5-MHz width. In this domain, the phase of each bin can be easily counter-rotated to correct for the fractional bitshift error caused by quantization of the delay offsets applied to the bitstreams.

The fringes at this point are still corrupted by instrumental phase shifts and instabilities. To calibrate these effects, calibration tones are injected during data-taking at the front of the instrumentation so that they will traverse the instrumentation along with the natural source signal and will be imbedded in the recorded signal. The first version of a calibration system using tones was developed by Rogers [3]. While the bitstreams are being cross-correlated for each baseline, each bitstream is also counter-rotated separately on the basis of tone model phase in order to extract the phase of each phase-calibration tone (phase-cal tone). The resulting tone-phase values are used to counter-rotate the frequency-domain fringes for each frequency bin in order to remove instrumental phase effects and thereby make the fringes coherent between RF channels.

After these corrections, the correlator sums the fringes in each frequency bin over a number of time points to compress the data further. The integration time covered in this sum should be no greater than $1/12^{th}$ the period of the highest expected residual fringe rate if amplitude loss is to be restricted to 1% or less. The separation between output fringe points will typically be 1-10 seconds.

After the fringes leave the correlator, the Tensor software performs a fast Fourier transform (FFT) over frequency and time, as illustrated in Fig. 5. First, the Tensor subsystem coherently sums the fringes over channels (four bins per channel) within a band by means of an FFT, which transforms the fringes from the (RF) frequency domain to the BWS-delay domain. The effect of this transform is to synthesize a bandwidth covering the RF band (e.g., 8300-8700 MHz). The BWS technique was developed by Rogers [4] to provide lower detection thresholds and more accurate delay measurements. Following the BWS FFT, an FFT over the time variable (e.g., over 200 seconds) transforms the fringes to the phase-delay-rate domain (fringe-frequency domain). For each RF band, the resulting fringes are then a complex function of the FFT variables (i.e., the search variables of BWS delay and fringe frequency), a function that peaks at the actual delay and delay rate. (One also has the option of transforming the fringes over only one axis, either frequency or time, and outputting the resulting array without estimating delay or delay rate.)

Signal detection consists of a search over the BWS delay and fringe frequency to find the maximum fringe amplitude (root-sum-square (RSS) of real and imaginary parts). To improve efficiency, the range of BWS delay and fringe frequency values covered in the search can be narrowed on the basis of a priori estimates, if desired.

In the post-Tensor software, the final observables (amplitude, BWS delay, phase delay, and phase-delay rate) for each band (e.g., S- and X-band) are extracted by means of a multiparameter least-squares fit of a fringe model to the fringes observed in the region of maximum amplitude. The fringe model used in the fit is computed as a coherent sum of phasers whose time-independent amplitudes can be separately specified for each channel by the user and whose phases are a linear function of BWS delay, phase-delay rate, and phase delay, all referenced to a time near the center of the observation and to an RF frequency near the center of the spanned bandwidth. After estimation, the post-Tensor software restores the model delay removed by the correlator, thereby producing total output values for BWS delay, phase-delay and phase-delay rate that are theoretically free of processing effects.

In spectral line applications, more than eight lag offsets are required to obtain adequate RF frequency resolution. For the BLKII processor, the number of lags per channel can be increased by decreasing the number of channels and using the correlators of the omitted channels to process more lags for the remaining channels. In the extreme case of one channel, 224 (28*8) lag offsets can be applied, which leads to a sample spacing of approximately 2000/112 = 18 kHz across the 2-MHz passband.

Another BLKII feature useful in astronomy applications is the capability of simultaneously processing right-circularly polarized and left-circularly polarized data. In this mode, each (RF) frequency channel is recorded on two tracks rather than one, so that a maximum of 14 channels can be recorded on MKIII tapes. Since cross-correlation of a given channel-pair now requires four combinations (R*R, R*L, L*R, L*L) rather than one, a maximum of seven (28/4) channels of polarized data can be cross-correlated in a single pass through the processor. With more than eight lags per pair, even fewer channels could be processed in a single pass.

SECTION III

IMPROVEMENTS

Many features of the BLKII processor represent significant improvements relative to its predecessor, the BLK0 processor. These include:

a) More (2-MHz) channels (28 rather than 8).

b) A higher total bit rate through continuous processing of each (2-MHz) channel.

c) An improved correction for bitstream-offsetting ("retarded station") effects.

d) An improved fractional-bitshift correction through more frequent (every 25 msec) application.

e) Better phase calibration by frequently (every 25 msec) applying intra-passband corrections.

f) Reduced intermodulation and aliasing in counter-rotated calibration-tone phase (cal-tone phase) by quantizing the tone-stopping sinusoids to 128 amplitude levels rather than 3.

g) Simpler and faster delay estimation, as well as a lower fringe detection threshold, by coherently summing the fringes from intrapassband bins across all channels in a band.

h) Improved capability for spectral line applications by cross-correlating as many as 224 lags.

The BLKII processor could be improved in a number of ways. Possible improvements include:

a) Increasing the number of stations to seven (and with more effort, to any number), including the associated 21 baseline correlators.

b) Increasing the number of phase-cal correlators from one to two (or four) per channel, which would allow more frequent (or continuous) sampling of calibration phase.

c) Increasing the delay lines to 0.5 sec (an improvement required for interferometry between a ground-based antenna and an orbiting satellite).

d) Applying a digital filter to the time sequence of counter-rotated fringes from each frequency bin in order to minimize the output sample rate in time.

e) Improving Tensor to increase the allowed range of uncertainty on a priori values for baselines and source positions.

Future resources will determine when these improvements will be implemented.

SECTION IV

CLOCK MODELING

Before proceeding to cross-correlation analysis, it will be helpful to define a few time-keeping terms. First, define the following thus:

t = true time (e.g., "perfect" universal time, coordinated (UTC))

ω_t = true oscillator frequency (relative to true time)

ω_c = nominal oscillator frequency (e.g., 5 MHz)

Throughout this analysis, true time will serve as the "foundation" of timekeeping since, in a nonrelativistic analysis, it is the uniform time scale applicable to both antennas.

Two "clocks" will be defined to assist in the analysis. The time of the first clock, the "recorder clock," is registered by the bits of the tape. This bit time is given in terms of true time by

$$t_b = t + \tau_b \tag{4.1}$$

where τ_b is the error in the recorder clock.

The second clock, the "ϕ-cal clock," will be established, at least conceptually, near the point where the 5-MHz signal from the station enters the phase calibrator instrumentation, as schematically illustrated in Figure 6. The phase at this reference point is given in terms of true frequency by

$$\phi_c = \omega_t(t - t_o) \tag{4.2}$$

where t_o is the (unknown) true time at which $\phi_c = 0$. As implied by Eq. 4.2, we will assume that the oscillator is perfectly stable so that the only imperfections in the station clock are offsets in epoch and rate. If phase ϕ_c is measured at the reference point, ϕ-cal time can be defined by

$$t_c = \phi_c/\omega_c \tag{4.3}$$

where we assume t_c is zero when ϕ_c is zero. This is possible since a particular zero crossing can be defined to be $t_c = 0$. If the nominal frequency is related to the true frequency by

$$\omega_c = \omega_t + \Delta\omega_c \tag{4.4}$$

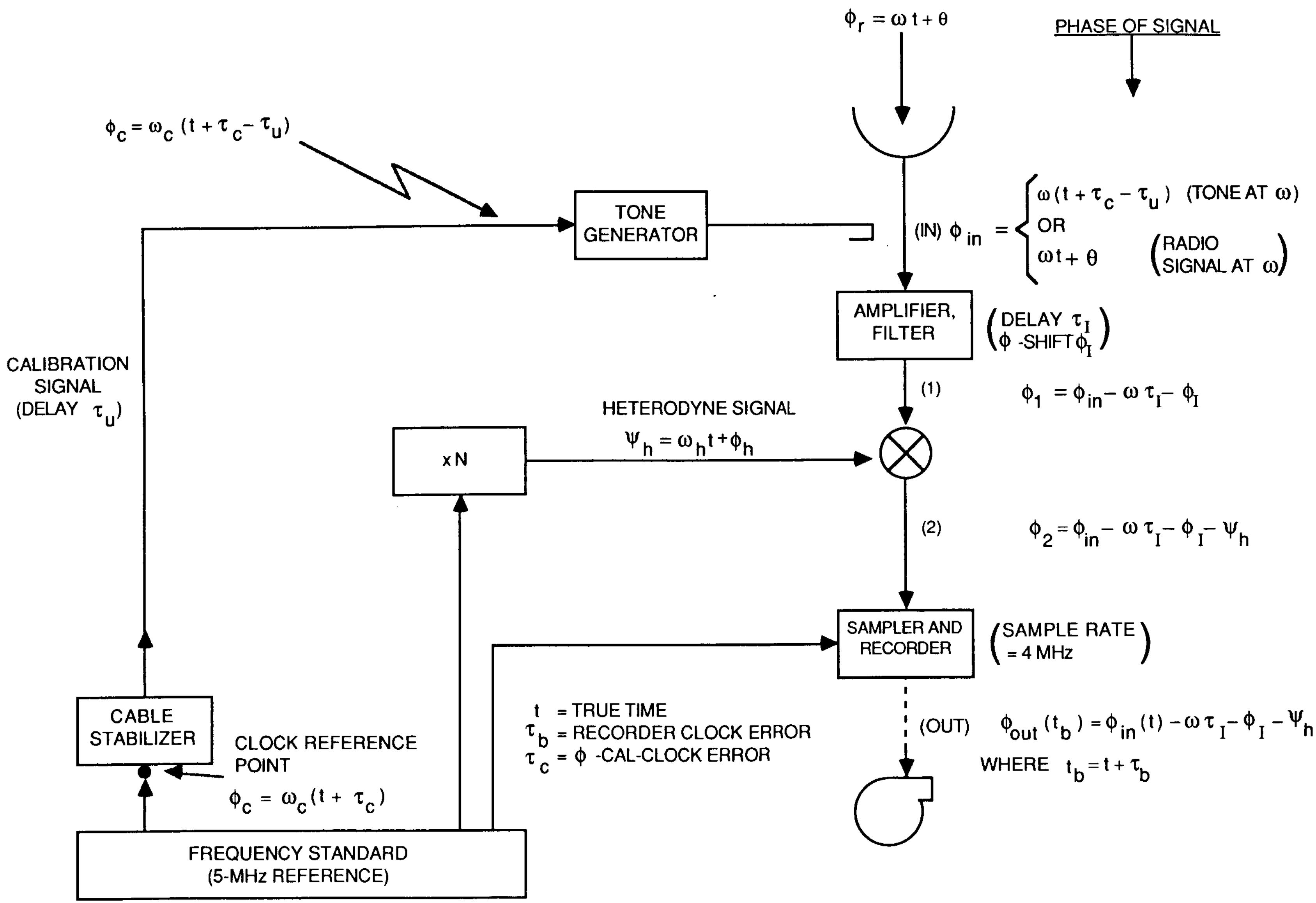

Figure 6. Simplified Illustration of Antenna Instrumentation

then ϕ-cal time is related to true time by

$$t_c = t + \tau_c \tag{4.5}$$

where the error in the ϕ-cal clock is given by

$$\tau_c = - \frac{\Delta\omega_c}{\omega_t} (t - t_o) - t_o \tag{4.6}$$

Usually the difference between ω_c and ω_t is small, less than a part in 10^{11}.

It is conceptually and instrumentally convenient to define a clock in terms of a 1-pps signal that drives a counter to register the number of received pulses. To establish the 1-pps signal, a particular set of positive-going zero crossings (one every 5 x 10^6 crossings for 5 MHz) must be selected. (Equivalently, in Eq. 4.3, a definition of $\phi_c = 0$ must be made.) This arbitrary selection for the ϕ-cal clock leads to an ambiguity which must be resolved in clock-synchronization measurements, as discussed in Section XIII. In this report, clock synchronization will be specified relative to the ϕ-cal clocks.

SECTION V

THE RECORDED NATURAL SOURCE SIGNAL

This section derives an expression for the analog signal by tracking the incoming signal from its free-space form through the instrumentation to its final form at baseband. Only non-relativistic theory will be considered in this report.

In typical radio interferometry measurements, two antennas simultaneously receive the signal produced by a very distant, compact natural source of random radio emissions. In this section, it will be assumed that the source is a point source. Effects caused by extended structure are derived in Appendix A and will be accounted for in the next section. Due to the great distance of the natural source, the incoming signal can be modeled by plane waves. Typical natural sources used in JPL applications emit noise with a smooth frequency distribution. A given member of the random ensemble of possible noise waves can be modeled as a superposition of plane waves of different frequencies:

$$E(\vec{x},t) = \int_{-\infty}^{\infty} A(\omega)\ e^{i[\omega t - \vec{k}\bullet\vec{x}]} d\omega \qquad (5.1)$$

where E is the electric field at true time t and at point x, $\vec{k} = \omega\hat{k}/c$ is the apparent wave vector of the plane wave, and $A(\omega)$ is the (random) Fourier amplitude at frequency ω. All quantities are measured with respect to a frame (the "geocentric frame") whose origin is at the center of mass of the earth and whose axes are defined by true equatorial coordinates of date. Frequency ω is specified in the geocentric frame on the basis of true time. The adjective "apparent" refers to the aberration effect that will be observed in a geocentric frame. For simplicity, the wave is assumed to be linearly polarized. At this point, it will be assumed that the wave propagates in a vacuum. Transmission media delays will be added in the next section.

Relative to geocentric coordinates, the electric field at a given station becomes

$$E_j(t) = E(\vec{x}_j(t),t) = \int_{-\infty}^{\infty} A(\omega)\ e^{i[\omega t - \vec{k}\bullet\vec{x}_j(t)]} d\omega \qquad (5.2)$$

where $\vec{x}_j(t)$ is the location of station j as a function of true time t. We will assume that each antenna is a parabolic dish with two rotation axes, and that station location is defined to be the intersection of those axes. For some antennas, the axes of rotation do not intersect and a correction [5] must be applied to the observed delay to establish an effective intersection of axes. This report will ignore possible axis offsets under the assumption that corrections will be applied in subsequent processing, if necessary.

After injection, the signal passes through several filters and is heterodyned to baseband under the combined effect of various mixing signals. The phase effects of all intervening components can be grouped into three catagories. First, the overall effect of the mixing signals can be described by one total mixing phase, $\omega_{hj}t + \phi_{hj}$, where ω_{hj} is the total mixing frequency and ϕ_{hj} represents both a constant phase offset and all variations in mixing phase that are nonlinear in time. Second, all group delays after the injection point, including effective group delays through filters, can be represented by one total delay, τ_{Ij}. Third, all remaining instrumental phase shifts can be represented by one total shift, ϕ_{Ij}. As implied, this frequency-dependent term contains all phase shifts left after accounting for the heterodyne phase and the effective group delay term τ_{Ij}.

Another "instrumental" delay, τ_{aj}, will be included below to establish the definition of antenna location. This delay, the "antenna" delay, is equal to the difference in path length for the radio wave in its actual propagation to the tone injection point and its theoretical propagation to the intersection of axes. Since the antenna continually rotates to point at the source, the injection point and the intersection of axes will have the same geocentric velocity and there will be no difference in the doppler shift at those two points. Thus, to include the antenna delay, one merely offsets the plane wave phase by a constant phase shift equal to the antenna delay expressed in terms of RF wavelength. It will be assumed in this report that the antenna delay is constant for all times and all sources and that dispersive phase shifts above the phase-calibration injection point are negligible. If either of these assumptions is not valid, then additional calibrations will be required to remove these effects.

Figure 6 schematically illustrates the modifications applied to the signal phase as the signal progresses through the station instrumentation from injection to the recorder. The block diagram has been grossly simplified to show only one element of each type, with token phase shifts and group delays. Nevertheless, the following analysis is quite general if the variables discussed above are properly defined to represent lumped effects of all elements in the actual station instrumentation. For more details concerning the MKIII data acquisition system, see [2].

When lumped instrumental effects are included, the doppler-shifted analog signal at baseband for a given BWS channel at station k at bit time t_{bk} can be written in the form:

$$V_k(t_{bk}) = \int_0^\infty A(\omega) G_k(y_k)\ e^{i\theta_k}\ d\omega + \text{c.c.} + \eta_k \qquad (5.3)$$

where

$$y_k \equiv \omega(1 - \hat{k} \cdot \dot{\vec{x}}_k/c) \qquad (5.4)$$

$$\theta_k \equiv \omega(t_{pk} - \tau_{ak}) - \vec{k} \cdot \vec{x}_k(t_{pk}) - \omega_{hk} t_{pk} - \phi_{hk} - \phi_{Ik}(y_k) \qquad (5.5)$$

In this expression, G_k is the amplitude of the system bandpass, η_k is the additive noise, y_k is the doppler-shifted (station) frequency corresponding to (geocentric) frequency ω, and c.c. denotes the complex conjugate. The time argument, t_{pk}, is the true time at which the signal recorded at bit time t_{bk} reached the phase-cal injection point. This time tag is computed from bit time by means of the relation:

$$t_{pk} = t_{bk} - \tau_{bk} - \tau_{Ik} \qquad (5.6)$$

where τ_{bk} is the error in bit time and τ_{Ik} is the total instrumental group delay from the injection point to the recorder. This time tag convention is established so that station locations can be specified in terms of true time when required in very accurate applications. Note that the antenna delay, τ_{ak}, does not affect the time tag calculation for $\vec{x}_k(t)$ since, as mentioned above, the correction to the observed delay to account for the antenna delay (unlike the correction to the observed delay to account for the time tag effects of τ_{bk} and τ_{Ik}) is essentially an additive constant for all times and sources. Thus, the antenna delay is an important consideration in clock synchronization but not in computation of station position. Because of this feature of the antenna-delay correction, the functions $\vec{x}_k(t_{pk})$ can be viewed as the location of the intersection of axes at t_{pk}, the true time corresponding to bit time t_{bj}.

The baseband signal is sampled at a rate equal to approximately twice the baseband bandwidth and recorded in a bilevel mode. That is, one bit is recorded for each sample point and that bit is 1 if the signal is positive and 0 if the signal is negative. Subsequent analysis will ignore that code and act as though +1 or -1 were directly recorded on the tapes. A tilde over the voltage symbol will be used to denote two-level quantization. For purposes of analysis, it will be assumed that the record rate is 4 Mbits/sec.

Before proceeding to cross-correlation analysis, we will reformulate the expression for the analog signal so all components are normalized in measurable units of noise temperature. For station k, let the normalized analog signal corresponding to V_k be given by

$$z_k(t) = \left[\sqrt{T_{qk}}\,q_k(t) + \sqrt{T_{nk}}\; n_k(t)\right] \Big/ \sqrt{T_{sk}} \qquad (5.7)$$

where z, q, and n are the total signal, natural source signal (the first two terms in Eq. 5.3) and additive noise (the last term in Eq. 5.3), respectively. We will assume these quantities are all normalized so that

$$\langle z^2 \rangle = \langle q^2 \rangle = \langle n^2 \rangle = 1 \qquad (5.8)$$

where ⟨⟩ denotes an ensemble average over all possible noise forms. The quantities T_s, T_q, and T_n are the (average) noise temperatures for the total signal, the natural source, and the additive noise, respectively. For the continuum sources typically observed in geophysical applications, it will be assumed that the source temperature is fairly constant across the (2-MHz) passband so that one average temperature can describe the whole passband. (The noise power per passband is actually kT_sW, but the factor kW drops out in the ratios.) As we shall see, the normalized form in Eq. 5.7 is more convenient for cross-correlation analysis. The noise temperature of the source can be obtained from source flux through the relation

$$T_{qk} = \kappa_k \, S_F \qquad (5.9)$$

where S_F is the total source flux in janskies and κ_k is the antenna sensitivity station k in kelvins/jansky.

SECTION VI

CROSS-CORRELATION

The BLKII correlator aligns the bits on the two tapes, multiplies them bitwise and fringe-stops (counter-rotates) the resulting fringes, as illustrated in Figs. 3 and 4. This section develops a detailed mathematical model for the cross-correlation function, the expectation value (ensemble average) of the product of the aligned signals. The expectation value is analyzed to remove statistical fluctuation in both signal and noise and thereby reveal the average behavior of the cross-correlated signal. Only one frequency channel will be explicitly analyzed even though the other channels are processed in parallel.

For station k, the unretarded delay model is computed as

$$\tau^{u}_{mk}(t) = -\frac{\hat{k}_m \bullet \vec{x}_{mk}(t)}{c} - \tau^{m}_{tk}(t) - \tau^{m}_{ck}(t) + \Delta_k, \quad k = i \text{ or } j \qquad (6.1)$$

in which the first term is the geometric delay relative to the earth's center of mass, expressed in terms of the modeled values for station location $\vec{x}_{mk}$ and apparent wave direction $\hat{k}_m$ (with both in geocentric coordinates). The term τ^m_{tk} models the troposphere delay ($\propto$ 1/sin EL), while τ^m_{ck} models the station clock error (including offset and rate). The delay Δ_k, which is specified below, represents one of two fixed integer-bit offsets required to center the fringes in the range of lag offsets.

For station k, the retarded delay $\tau_{mk}(t)$ used to offset the bitstream is computed as

$$\tau_{mk}(t) = \tau^{u}_{mk}\,(t - \tau_{mk}) \qquad (6.2)$$

where τ_{mk} is obtained by iteration, beginning with $\tau_{mk} = \tau^{u}_{mk}$. As will be shown in Section VII, this method for retarding the model delay compensates for the effect of bitstream offsetting on the time tag of geometric and tropospheric components of the actual phase.

To obtain the total bitstream offset, the correlator rounds the retarded model delay in Eq. 6.2 to the nearest bit, which will be denoted by a tilde over τ_{mk}. In Fig. 3, the delay τ'_m refers to the first three terms in Eq. 6.1, while the delay τ_m includes the fixed delay Δ_k following τ'_m.

The correlator offsets the signals recorded at the two stations and multiplies them, as illustrated in Figs. 3 and 4. The ensemble average of this product, the cross-correlation function, is defined by

$$r(t_G,\ell) \equiv \langle \tilde{V}_i(t_{bi} - \tilde{\tau}_{mi}(t_G) - \ell b)\ \tilde{V}_j(t_{bj} - \tilde{\tau}_{mj}(t_G)) \rangle \qquad (6.3)$$

where $\tilde{V}_k(t_{bk})$ is the recorded (two-level) voltage at bit time t_{bk} at station k; $\tilde{\tau}_{mi}$ and $\tilde{\tau}_{mj}$ are the quantized model delays used to offset the two bitstreams; and ℓ is any one of eight lag offsets (ℓ = 0 to 7) applied to station i. For a record rate of 4 Mbits/sec, the bit interval b is equal to $(4\ \text{Mbit/sec})^{-1}$ = 250 nsec. The quantized model delays are obtained by rounding to the nearest bit the delay values computed from Eq. 6.2 at time t_G. As mentioned above, the delays τ_{mi}, τ_{mj} each include a fixed delay, Δ_k, applied by the correlator. The fixed delay is equal to 2 bits for station i and 5 bits for station j. Based on these values for the fixed delays, the peak lag is nominally $\ell = 3$. As explained in [1], p. 69, the correlator applies to the bitstream of station i a pairwise vernier delay equal to (-1, 0, or + 1) bit in order to compensate whenever single-station rounding is inappropriate for pairwise offsetting. The vernier delay is implicitly contained in $\tilde{\tau}_{mi}$ in Eq. 6.3. Note, however, that the fixed delay and vernier delay are applied together in actual correlator operation, as shown in Fig. 3.

The argument t_G is the common Greenwich time defined by the bits on the two tapes. That is, the correlator implicitly enforces the assumption that

$$t_{bi} = t_{bj} \equiv t_G \qquad (6.4)$$

and uses t_G as the time tag. Corrections are applied in Section XII to account for time tag errors introduced by this assumption.

For a small correlation amplitude ($r \ll 1$), the van Vleck relation [6] gives the cross-correlation function in Eq. 6.3 in terms of the analog signals:

$$r(t_G,\ell) = \frac{2}{\pi} \frac{\langle V_i(t_{bi} - \tilde{\tau}_{mi} - \ell b)\ V_j(t_{bj} - \tilde{\tau}_{mj}) \rangle}{\sqrt{\langle V_i^2 \rangle \langle V_j^2 \rangle}} \qquad (6.5)$$

(In typical VLBI measurements, one finds $r < 0.2$.) With the normalized representation of the preceding section, the expectation of the normalized voltage product in Eq. 6.5 becomes

$$\frac{\langle v_i(\hat{t}_{bi})\ v_j(\hat{t}_{bj})\rangle}{\sqrt{\langle v_i^2\rangle \langle v_j^2\rangle}} \equiv \langle z_i(\hat{t}_{bi})\ z_j(\hat{t}_{bj})\rangle \tag{6.6}$$

$$= \sqrt{\frac{T_{qi}\ T_{qj}}{T_{si}\ T_{sj}}}\ \langle q_i(\hat{t}_{bi})\ q_j(\hat{t}_{bj})\rangle \tag{6.7}$$

since the additive noise n_j is uncorrelated between stations. The abbreviated notation for the arguments is defined by

$$\hat{t}_{bi} \equiv t_{bi} - \tilde{\tau}_{mi} - \ell b \tag{6.8}$$

$$\hat{t}_{bj} = t_{bj} - \tilde{\tau}_{mj} \tag{6.9}$$

Thus the problem is reduced to computing the correlation between the normalized natural source components (q_k) for the two stations, with the overall amplitude scaled by a multiplicative system temperature factor. Note that this factor times $2/\pi$ gives the amplitude of the cross-correlation function for perfectly correlated natural source components (i.e., $\langle q_i q_j\rangle = 1.0$).

We will now present on the basis of a plausibility discussion the final form for the cross-correlation function. A complete derivation is given in Appendix A, including the effects of source structure and the random nature of the source signal.

The natural source signal, q, is given by the first two terms in Eq. 5.3 but is normalized to have unit power. Thus the product $q_i\ q_j$ can be represented by a double integral over frequency where the integrand includes the sum of two products of the form $A(\omega)A^*(\omega')$ and $A(\omega)A(\omega')$. After the ensemble average, only the product $\langle A(\omega)A^*(\omega')\rangle$ has a non-zero value and this occurs as a delta function at $\omega = \omega'$. (It will be assumed that the signal from the natural source is stationary so that the amplitude at one frequency is uncorrelated with the amplitude at another frequency.) Thus, the double integral over frequency collapses to a single integral over frequency with one term in the integrand. If we let $S_p(\omega)$ denote the source power spectrum arising from $\langle A(\omega)A^*(\omega)\rangle$, the cross-correlation function becomes

$$r(t_G,\ell) \approx \frac{2}{\pi}\,\frac{r_m}{2}\,\frac{1}{D_N}\int_0^\infty S_p(\omega)\ G_i(y_i)\ G_j(y_j)\ e^{i\phi_f} d\omega + \text{c.c.} \tag{6.10}$$

where

$$r_m \equiv v_f \sqrt{\frac{T_{qi}\, T_{qj}}{T_{si}\, T_{sj}}} \tag{6.11}$$

$$D_N^2 \equiv \int_0^\infty S_p(\omega)\, G_i^2(y_i)d\omega \int_0^\infty S_p(\omega)\, G_j^2(y_j)d\omega \tag{6.12}$$

$$\begin{aligned}\phi_f = \phi_h &- \omega_{hj}\, \tilde{\tau}_{mj} + \omega_{hi}(\tilde{\tau}_{mi} + \ell b) \\ &+ \vec{k}_a \bullet \left[\vec{x}_j(t_{pj} - \tilde{\tau}_{mj}) - \vec{x}_i(t_{pi} - \tilde{\tau}_{mi} - \ell b)\right] \\ &+ \omega\left[\tau_b + \tau_I + \tau_a - \tilde{\tau}_{mi} + \tilde{\tau}_{mj} - \ell b\right] \\ &+ \phi_I + \phi_B + \phi_e \end{aligned} \tag{6.13}$$

in which

$$\phi_h \equiv (\omega_{hj}t_{pj} + \phi_{hj}) - (\omega_{hi}t_{pi} + \phi_{hi}) \tag{6.14}$$

and τ_b, τ_I, τ_a, and ϕ_I are differences between the corresponding station quantities in the order j minus i (e.g., $\tau_I = \tau_{Ij} - \tau_{Ii}$).

The instrumental phase shift, ϕ_I, is the difference of the instrumental shifts at the two stations, with each given an argument offset to account for doppler shifting:

$$\phi_I = \phi_{Ij}(y_j) - \phi_{Ii}(y_i) \tag{6.15}$$

As noted in Section V, ϕ_I represents nonlinear terms in the phase-frequency response of the instrumentation, while the delay τ_I represents linear terms. The linear terms will be accounted for when the "time tag" correction is applied (see Section XII). The current phase-calibration procedure will remove phase effects to first approximation but does not account for doppler shifting in the nonlinear terms. If all channels have matched phase-frequency responses, this doppler effect would essentially cancel in the BWS delay. This potential error source will not be treated in this report, but it might be large enough in some applications to require correction.

The amplitude terms in the cross-correlation function in Eq. 6.9 can be explained as follows. The factor of $2/\pi$ is the amplitude loss due to two-level sampling (see Eq. 6.5). The factor of 1/2 is a consequence of complex representation of the fringes and gives the proper definition for the power spectrum S_p (i.e., by cancelling the factor of 2 gained when the complex conjugate in Eq. 6.10 is added to obtain a real number for the cross-correlation function). Normalization of the signal in terms of system temperature generates the factor r_m, as suggested by the derivation of Eq. 6.7. Included in r_m is the fringe visibility v_f, which accounts for loss in fringe amplitude due to the resolving power of the interferometer. Fringe visibility can be expressed as

$$v_f = S_c/S_F \tag{6.16}$$

where S_c is the "correlated" flux of the source and S_F is the total flux. The fringe visibility and a brightness transform phase shift ϕ_B are two of the three modifications to the final cross-correlation function when the analysis is generalized to include extended sources as shown in Appendix A. The third modification is to change the point-source wave direction $\hat{k}$ to $\hat{k}_a$, a wave direction defined relative to a somewhat arbitrary reference point within the extended source.

In the denominator, the quantity D_N^2 is the product of the total source power from the two stations and arises from the normalization of the natural source components at each station (that is, from the requirement $\langle q_i^2\rangle = \langle q_j^2\rangle = 1$). Note that, as one would expect, the total source power at each station is equal to the integrated power across the passband where the power at each frequency is given by the spectral power of the natural source multiplied by the square of the bandpass amplitude.

Within the integral in Eq. 6.10, the various terms can be explained as follows. Since a component of the natural source signal at one frequency is uncorrelated with a component at any other frequency, the correlated signal can be obtained by multiplying each frequency component at one station by the corresponding component at the other station and then summing this product over all frequencies. By corresponding frequency components we mean the components with the same frequency in geocentric coordinates. Due to the earth's rotation, a given geocentric frequency will be doppler-shifted when measured by station instrumentation. Those shifts are accounted for by the doppler-shifted arguments y_k in the bandpass functions G_k and in the phase shifts ϕ_{Ik}.

Since interferometers are differencing devices, the phase ϕ_f in Eq. 6.13 is the difference in the frequency-specific phase for the two stations, each with the offset in time introduced by correlator delays. All of the phase terms in Eq. 6.13 can be derived in this manner except for three which involve special considerations. First, as mentioned above, the brightness transform phase ϕ_B is a consequence of source structure as shown in Appendix A. Second, the quantities τ_b and τ_I arise from the difference $t_{pi} - t_{pj}$, which, through the use of Eqs. 5.6 and 6.4, can be shown to equal

$$t_{pi} - t_{pj} = \tau_b + \tau_I \tag{6.17}$$

Third, a phase term ϕ_e has been added in Eq. 6.13 to account for differential ionosphere effects, with the station difference in the order j minus i.

Introduction of an "interim" delay, τ_x, simplifies the expressions for the fringe phase in Eq. 6.13:

$$\begin{aligned}\phi_f &= \phi_h - \omega_{hj}\tilde{\tau}_{mj} + \omega_{hi}(\tilde{\tau}_{mi} + \ell b) \\ &\quad + \omega\left[\tau_x + \tau_b + \tau_I + \tau_a - \tilde{\tau}_{mi} + \tilde{\tau}_{mj} - \ell b\right] \\ &\quad + \phi_I + \phi_B + \phi_e\end{aligned} \tag{6.18}$$

The interim delay is defined by

$$\tau_x \equiv \tau_{di}(t_{pi} - \tilde{\tau}_{mi} - \ell b) - \tau_{dj}(t_{pj} - \tilde{\tau}_{mj}) \tag{6.19}$$

where

$$\tau_{dk}(t) \equiv -\frac{\hat{k}_a \bullet \vec{x}_k(t)}{c} - \tau_{tk}(t), \quad k = i \text{ or } j \tag{6.20}$$

Note that the definition of interim delay has been expanded here to include the troposphere delay τ_{tk}, which had been neglected to this point.

The phase rate $\dot{\phi}_f$ can reach about 20 kHz at X-band. Therefore, before the data can be compressed by summing over bits, the fringe phase must be counter-rotated to a very low rate (< 0.1 Hz). The next section discusses that procedure.

SECTION VII

FRINGE COUNTER-ROTATION

In most observations of natural sources, the system noise is much greater than the correlated amplitude so that the signal-to-noise ratio (SNR) for a single bit product (Eq. 6.3) is very small (0.0002 - 0.2). Thus many bits of data ($\sim 10^3$ - 10^9) must be collected to raise the SNR to a usable level on the integrated signal. However, due to the high phase rate that the fast fringes typically possess (as high as 20 kHz at X-band), the data volume cannot be compressed by directly summing the fringes over time (bits). This section explains fringe stopping, a process that counter-rotates the fringes (i.e., digitally heterodynes the fringes to a low frequency) and thereby allows successive sums over time with each sum compressing a correlation interval of 25 msec (10^5 bits) into one point (stopped fringes or correlation coefficient). In addition to permitting a massive data compression, counter-rotation can, with modification, partially remove the effects of model-delay quantization and of bitstream offsetting.

To avoid significant losses in output fringe amplitude, the model phase used to counter-rotate must be constructed with sufficient accuracy to insure that only a small fraction of a cycle is traversed by the stopped fringes over the total integration interval. (As indicated in the next two sections, the stopped fringes are ultimately summed over a time interval that might be of the order of 1-10 sec.) For example, if the geometric delay, the component with the greatest uncertainty, is known to a part in 10^6 (e.g., a 0.2 arcsec position error), then the stopped phase will change by $20\ \text{kHz} \cdot 10^{-6} \cdot 1\ \text{sec} = 0.02$ cycle across the integration interval when the fringe rate is at its maximum value of 20 kHz at X-band and the integration time is 1 sec. Amplitude loss due to a 0.02 cycle change in phase is only 0.07 percent. It will be assumed that amplitude loss due to the inaccuracy of the fringe model is negligible.

The model phase used for fringe counter-rotation is identical in form to the BLK0 model and is given by

$$\phi_m(t_G) = (\hat{\omega}_{hj} - \hat{\omega}_{hi})(t_G - t_s) - \hat{\omega}_{hj}\,\tilde{\tau}_{mj}(t_G) + \hat{\omega}_{hi}\,\tilde{\tau}_{mi}(t_G)$$
$$+ \hat{\bar{\omega}}\left[\tilde{\tau}_{mj}(t_G) - \tau_{mj}(t_G) - \tilde{\tau}_{mi}(t_G) + \tau_{mi}(t_G)\right] \qquad (7.1)$$

where $\hat{\omega}_{hk}$ is the best estimate for the total mixing frequency, ω_{hk}, and $\hat{\bar{\omega}}$ is close to the centroid frequency of the 2-MHz passband. The time t_s is a reference time adopted at the correlator and usually marks the start of the observation. Note that the delay for station i is set equal to the "$\ell = 0$" value, which means the same counter-rotation phase is used for all lag offsets. The variation of fringe phase with lag (i.e., in τ_x) will be removed below.

To counter-rotate, the voltage product in Eq. 6.3 is multiplied at each bit by a phaser based on Eq. 7.1 and summed over the time points (bits) within a correlation interval, producing one complex value for that interval:

$$u_\ell(t_G) = \sum_{t'_G} \tilde{V}_i(t'_G - \tilde{\tau}_{mi} - \ell b)\, \tilde{V}_j(t'_G - \tilde{\tau}_{mj})\, e^{-i\phi_m(t'_G)} \qquad (7.2)$$

This process is illustrated in Fig. 3. The counter-rotation sum covers an interval of 100,000 bits (25 msec), during which the bitstream offsets $\tilde{\tau}_{mi}$, $\tilde{\tau}_{mj}$ remain constant. The time argument t_G now refers to the time at the middle of the sum interval.

The BLKII correlator, like the BLKO correlator, approximates the fringe counter-rotation sinusoids with three-level (-1, 0, +1) functions (see p. 19 in [1]). We will assume that the only modification introduced in the stopped cross-correlation function by this quantization is a small increase in amplitude, which will be applied below. Fringe SNR is reduced about 4 percent by this quantization. A simplified example of counter-rotation in terms of bits is shown in Figure 4 for an artificially short integration interval of 8 bits.

By combining Eq. 7.2 with the expectation value in Eq. 6.3, one finds that the expectation value for the complex stopped fringes is given by

$$\langle u_\ell(t_G)\rangle = \sum_{t'_G} r(t'_G, \ell)\, e^{-i\phi_m(t'_G)} \qquad (7.3)$$

When Eq. 6.10 is substituted for $r(t, \ell)$, two terms result: a sum-frequency term and a difference-frequency term. For sufficiently high fringe rates ($\dot{\phi}_f >> 100$ Hz), the sum-frequency term essentially averages to zero in the sum over time, leaving only the difference term:

$$\langle u_\ell(t_G)\rangle = \frac{1}{\pi}\frac{r_m}{D_N}\sum_{t_G'}\int_0^\infty S_p(\omega)\, G_i(y_i)\, G_j(y_j)\, e^{i\Delta\phi_f} d\omega \qquad (7.4)$$

where the stopped phase is given theoretically by

$$\Delta\phi_f = \phi_f - \phi_m \qquad (7.5)$$

$$= \Delta\phi_h + \omega\Delta\tau_R'' + \phi_I + \phi_B + \phi_e$$

$$- (\omega - \omega_{hi})\, \ell b + (\omega - \hat{\bar{\omega}})\, (\tau_m - \tilde{\tau}_m) \qquad (7.6)$$

for which we have made the definitions

$$\Delta\tau_R'' \equiv \tau_x + \tau_b + \tau_I + \tau_a - \tau_m \qquad (7.7)$$

$$\tau_m \equiv \tau_{mi}(t_G) - \tau_{mj}(t_G) \qquad (7.8)$$

$$\tilde{\tau}_m \equiv \tilde{\tau}_{mi}(t_G) - \tilde{\tau}_{mj}(t_G) \qquad (7.9)$$

$$\Delta\phi_h \equiv \phi_h - (\hat{\omega}_{hj} - \hat{\omega}_{hi})\, (t_G - t_s) \qquad (7.10)$$

Two terms of the form $(\hat{\omega}_{hj} - \omega_{hj})\, \tilde{\tau}_{mj}$ that are of the order of 10^{-4} cycle or less have been omitted.

The delay offsets ($\tilde{\tau}_{mi}$ and $\tilde{\tau}_{mj}$) applied to the two bitstreams introduce implicit effects in fringe phase that enter primarily in the time dependence of the actual geometric and tropospheric delays. One can readily demonstrate that model delay and phase have been constructed to approximately remove these effects. Expand both the interim delay in Eq. 6.19 and the model delay in Eqs. 6.2 and 7.8 about their time arguments and insert these expansions in the residual delay in Eq. 7.7 to obtain

$$\Delta\tau_R'' = \tau_{di}(t_{pi}) - (\tilde{\tau}_{mi} + \ell b)\dot{\tau}_{di} - \tau_{dj}(t_{pj}) + \tilde{\tau}_{mj}\,\dot{\tau}_{dj}$$

$$- \tau^u_{mi}(t_G) + \tau_{mi}\,\dot{\tau}^u_{mi} + \tau^u_{mj}(t_G) - \tau_{mj}\,\dot{\tau}^u_{mj} + \tau_b + \tau_I + \tau_a \tag{7.11}$$

By design, all but one of the first-order terms in Eq. 7.11 cancel if one neglects the small difference ($\sim 10^{-12}$) between $\dot{\tau}_{dk}$ and $\dot{\tau}^u_{mk}$ and neglects the quantization error (i.e., $\dot{\tau}_{dk} \bullet (\tau_{mk} - \tilde{\tau}_{mk}) \lesssim 1.6 \bullet 10^{-6} \bullet 125$ nsec $= 0.2$ psec). With these approximations, one obtains a residual delay independent of correlator offsets except for a small term dependent on ℓ:

$$\Delta\tau_R'' = \tau_{di}(t_{pi}) - \tau^u_{mi}(t_G) - \tau_{dj}(t_{pj}) + \tau^u_{mj}(t_G)$$

$$- \dot{\tau}_{di}\ell b + \tau_b + \tau_I + \tau_a \tag{7.12}$$

Removal of the ℓ-term will be discussed in the next section. The remaining differences in arguments due to clock synch errors (i.e., t_G vs. t_{pi} or t_{pj}) cause very small delay errors that are considered in Section XII.

The theoretical expression for the stopped fringes can be re-written by interchanging the sum and integral in Eq. 7.4 to obtain

$$\langle u_\ell(t_G)\rangle = N_t \frac{a_1}{\pi} \frac{r_m}{D_N} \bullet$$

$$\int_0^\infty S_p(\omega)\, G_i(y_i)\, G_j(y_j)\, F_q\, e^{i[\psi_f - (\omega - \omega_{hi} + \omega\dot{\tau}_{di})\ell b]}\, d\omega \tag{7.13}$$

where the "quantization filter" ("fractional-bitshift filter") is defined by

$$F_q(\omega-\hat{\bar{\omega}}) = \frac{1}{N_t} \sum_{t_G'} e^{i(\omega-\hat{\bar{\omega}})\,(\tau_m - \tilde{\tau}_m)} \qquad (7.14)$$

and where the residual fringe phase is given by

$$\psi_f(\omega,t_G) = \Delta\phi_h + \omega\Delta\tau_R' + \phi_I + \phi_B + \phi_e \qquad (7.15)$$

in which the residual delay is defined by

$$\begin{aligned}\Delta\tau_R' = {} & \tau_{di}(t_{pi}) - \tau_{mi}^u(t_G) - \tau_{dj}(t_{pj}) + \tau_{mj}^u(t_G) \\ & + \tau_b + \tau_I + \tau_a \end{aligned} \qquad (7.16)$$

N_t is equal to the number (10^5) of time points (bits) in the sum.

The factor $a_1 = 1.176$ has been inserted to account for the amplitude increase caused by quantization of the stopping sinusoid, as discussed above. The sum over time has been applied only to the "quantized-delay phaser" from the last term in Eq. 7.6, since the time variation of that factor will dominate when an accurate model delay is used. That is, the rate of the residual phase ($\dot{\psi}_f$) can be made very small (< 0.02 Hz) so that the stopped phase ψ_f will change by only a small amount (< 1 mcycle) over a sum interval (25 msec). On the other hand, the phase $(\omega - \hat{\bar{\omega}})(\tau_m - \tilde{\tau}_m)$ can change by as much as $(\omega - \hat{\bar{\omega}})\,\dot{\tau}_m\,\Delta t \lesssim 1$ MHz* 2 μsec/sec* 25 msec = 50 mcycle over a sum interval for a 2-MHz bandpass. As explained in Appendix D of [1], the quantization filter F_q can easily be calculated on the basis of delay quantization applied at the correlator. Exceptions to the above assumption of small residual rate can occur in "initialization" runs involving a poorly known baseline or source position. However, this will occur only for the first pass through the correlator since the results of that pass can be used to improve the a priori delay for all subsequent passes involving that baseline or source.

SECTION VIII

TRANSFORMING TO THE FREQUENCY DOMAIN

The lag-domain fringes in Eq. 7.13 are corrupted by instrumental phase shifts and by the fractional bitshift error resulting from quantization of the bitstream offsets. These effects can be easily removed through counter-rotation if the fringes are first transformed from the lag domain to frequency domain. Based on the assumption that the a priori delay model is accurate enough to place the maximum fringe amplitude near the center of the lag range, the fringes are transformed by means of a discrete Fourier transform (DFT) as follows:

$$h(\omega_k', t_G) = \sum_{\ell=0}^{N_\ell - 1} u_\ell(t_G)\, e^{i(\omega_k' + \varepsilon_k)\ell b} \tag{8.1}$$

where N_ℓ (= 8) is the number of lags and where ω_k' is any one of four baseband frequencies and ε_k is a tweak (doppler) frequency inserted to remove the effect of lag offsetting in the argument of the interim delay. The four baseband frequencies, ω_k', are placed within the 2-MHz passband approximately as follows: 0.25, 0.75, 1.25, and 1.75 MHz, where the sign is positive (negative) for the upper (lower) sideband. To compute the corresponding RF bin frequencies (ω_k), one must add the total mixing frequency (ω_{hi}) at station i to these baseband frequencies.

Details concerning the implementation of the DFT in Eq. 8.1 will not be presented in this report. That implementation involves a preliminary frequency-shift operation to properly place the final bin frequencies and to apply the ε_k correction, followed by a standard FFT over lag. In subsequent Tensor processing, it is assumed that all bin frequencies across the RF band fall on a uniform grid with 0.5 MHz between points. Thus, the L.O. frequency for each channel and the frequency shift mentioned above must be properly chosen to produce such placement of bin frequencies. If phase closure is desired and if the L.O. frequencies are slightly offset from one another around the baseline triangle, the frequency shift operation can be adjusted to produce the same bin frequencies, in RF terms, for all baselines.

The tweak frequency is given a value that will approximately remove the $\omega\dot{\tau}_{di}\ell b$ phase term in Eq. 7.13:

$$\varepsilon_k = (\omega_k' + \hat{\omega}_{hi})\, \dot{\tau}_{mi} \tag{8.2}$$

in which $\dot{\tau}_{mi}$ is the model delay rate for station i at the center of the 25-msec interval. In practice, one can replace ω_k + ω_{hi} in this expression with the centroid frequency, $\bar{\omega}$, with negligible loss of accuracy. For analysis purposes, however, the more exact expression in Eq. 8.2 will be used. The effect of this correction is to shift the output frequency spectrum by a small amount (< 20 kHz at X-band for earth-fixed antennas).

The expectation value of the DFT is given by

$$\langle h(\omega_k', t_G) \rangle = \sum_{\ell=0}^{N_\ell - 1} \langle u_\ell(t_G) \rangle e^{i(\omega_k' + \varepsilon_k)\ell b} \tag{8.3}$$

where the sign convention for frequency is as described above.

By substituting the expression for $\langle u_\ell \rangle$ found in Eq. 7.13 and interchanging the sum and integral, one obtains

$$\langle h(\omega_k', t_G) \rangle = N_t \frac{a_1}{\pi} \frac{r_m}{D_N} \int_0^\infty S_p(\omega)\ G_i(y_i)\ G_j(y_j)\ F_q\ S_T(\Delta\omega)\ e^{i\psi_f} d\omega \tag{8.4}$$

where the convolution function is given by

$$S_T(\Delta\omega) \equiv e^{i\Delta\omega(N_\ell - 1)b/2} \frac{\sin\ (\Delta\omega N_\ell b/2)}{\sin\ (\Delta\omega b/2)} \tag{8.5}$$

and the difference frequency by

$$\Delta\omega \equiv [\omega_k' + (\omega_k' + \hat{\omega}_{hi})\dot{\tau}_{mi}] - [\omega' + (\omega' + \omega_{hi})\dot{\tau}_{di}] \tag{8.6}$$

in which

$$\omega' = \omega - \omega_{hi} \tag{8.7}$$

The convolution function is centered on each frequency bin and represents a filter with a null-to-null width of $2/(N_\ell b)^{-1}$, which, for an 8-lag transform and a 4-Mbits/sec sample rate, equals 1 MHz. Because of this convolution, the output phase and amplitude (i.e., $h(\omega_k'))$ for a given DFT frequency ω_k' will not be precisely equal to the input cross-power spectrum at that frequency but will be equal to a weighted average of that spectrum around that frequency. As analyzed in Appendix E of [1], the phase discrepancies due to this effect are surprisingly small for an 8-lag transform. Given an "ideal" MRKIII bandpass shape (bandpass B in Table E1 of [1]), the difference between the phase of the convolved spectrum and the cross-power phase is less than 4 mcycles for each bin and less than 0.1 mcycle for the composite phase for the whole bandpass. Discrepancies in amplitude, on the other hand, are as high as 6% for individual bin amplitudes and 1.5% for the composite amplitude, where both percentages are relative to the maximum bandpass amplitude.

Since the phase errors introduced by the limited-lag transforms are generally not significant for the present system, let the number of lags approach infinity for the purpose of approximately determining the form of the transformed fringes. As the number of lags approaches infinity, the convolution function becomes

$$\lim_{N_\ell \to \infty} S_T(\Delta\omega) = 4\pi W \, \delta(\Delta\omega) \tag{8.8}$$

where $\delta(x)$ is the delta or impulse function and W is the recording bandwidth (2 MHz). As indicated by Eq. 8.6 for $\Delta\omega = 0$, the delta function enforces the following relation:

$$\omega' + (\omega' + \omega_{hi})\dot{\tau}_{di} = \omega_k' + (\omega_k' + \hat{\omega}_{hi})\dot{\tau}_{mi} \tag{8.9}$$

Since the lag-offset effect is small ($\omega\dot{\tau}_{di} < 20$ kHz at X-band), since $\hat{\omega}_{hi}$ is nearly equal to ω_{hi} (to 10^{-12}), and since the delay model is accurate, we readily see that the delta function chooses the following RF frequencies:

$$\omega_k = \omega_k' + \omega_{hi} \tag{8.10}$$

That is, the DFT outputs frequency-domain fringes at four frequency points whose RF values are equal to the four baseband values given in the first paragraph of this section plus the total heterodyne frequency of station i, ω_{hi}. For an infinite number of lags, the delta function in Eq. 8.8 can be substituted for S_T in Eq. 8.4 to obtain the output frequency-domain fringes:

$$\langle h(\omega_k', t_G)\rangle = N_t \frac{2}{\pi} a_1 r_m \frac{S_p(\omega_k)\ G_i(y_{ik})\ G_j(y_{jk})}{D_A} F_q\ e^{i\psi_f(\omega_k, t_G)} \tag{8.11}$$

where

$$D_A \equiv \frac{D_N}{2\pi W} \tag{8.12}$$

$$y_{ik} = \omega_k(1 - \hat{k} \bullet \dot{\vec{x}}_i/c) \tag{8.13}$$

and where

$$\psi_f = \Delta\phi_h + \omega_k \Delta\tau_R' + \phi_I + \phi_B + \phi_e \tag{8.14}$$

in which $\Delta\tau_R'$ is given by Eq. 7.16, the quantization filter F_q by Eq. 7.14, D_N by Eq. 6.12, and r_m by Eq. 6.11.

In the following analysis, we neglect the small discrepancies resulting from the limited-tag transform and use Eq. 8.11 to describe the fringes in the frequency domain. If necessary, the transformation discrepancies could be corrected to a large extent through modeling, but such measures will not be treated in this report.

When phase closure observables are formed in source structure measurements, processing effects must "close" (sum to zero) around the baseline triangle. Closure of processing effects requires antisymmetry in residual phase with respect to interchange of stations. Note that residual phase in Eq. 8.14 is antisymmetric with respect to interchange of the i and j subscripts except for one difference implicitly contained in $\Delta\tau_R$, namely $\Delta_j - \Delta_i$, which is always equal to +3 lags. To enforce antisymmetry in this difference, the fringes can be counter-rotated at each bin frequency by a phaser of the form $e^{-3i\omega_k b}$, which, in effect, changes the value of Δ_j from 5 to 2 bits. It will be assumed in subsequent analysis that such a rotation has been performed and that the value of Δ_j is changed to 2 bits in Eq. 6.1.

The DFT over lag has cast the fringes in a form in which the phase effects due to instrumentation and fractional-bitshift error are exposed as phase shift in each frequency-bin phaser. In this form, these unwanted effects can be removed through counter-rotation, as explained in the following sections.

SECTION IX

FRACTIONAL BITSHIFT CORRECTION

When the bitstreams are offset by the model delays, the offsets are rounded to the nearest integer bit. This rounding introduces a fractional bitshift error that ultimately shows up in Eq. 8.11 as an unwanted phase shift residing in the quantization filter, F_q (see Eq. 7.14). This section outlines the removal of the fractional-bitshift error in fringe phase.

Since the BLKII processor does not change the quantized delays (bitstream offsets) during a 25-msec counter-rotation sum, the quantization filter in Eq. 7.14 becomes

$$F_q(\omega_k - \hat{\bar{\omega}}) \approx \frac{\sin[(\omega_k - \hat{\bar{\omega}})\dot{\tau}_m T_c/2]}{\left(\omega_k - \hat{\bar{\omega}}\right)\dot{\tau}_m T_c/2}\, e^{i\theta_q} \qquad (9.1)$$

where T_c is the sum interval and $\dot{\tau}_m$ is evaluated at the center of the interval. For an integration time of 25 msec, a 2-MHz bandwidth, and an intercontinental value of 2 μsec/sec for $\dot{\tau}_m$, the sinx/x amplitude loss at the edges of the 2-MHz bandpass will be approximated by 0.5%. This small amplitude loss will be ignored in subsequent equations. The "fractional bitshift" phase in Eq. 9.1 can be derived from Eqs. 7.8, 7.9, and 7.14:

$$\theta_q = (\omega_k - \hat{\bar{\omega}})\left[\tau_{mi}(t_G) - \tau_{mj}(t_G) - \tilde{\tau}_{mi}(t_G) + \tilde{\tau}_{mj}(t_G)\right] \qquad (9.2)$$

where $\hat{\bar{\omega}}$ is the "center" frequency used in Eq. 7.1 and where t_G now refers to the center of the 25-msec interval.

This phase correction is the conventional fractional bitshift error (i.e., roundoff error) at the center of the 25-msec correlation interval. Since these phase terms are accurately known, they can be counter-rotated out of the fringes given in Eq. 8.11. The expectation value of the resulting fringes is given by

$$\langle h'(\omega_k, t_G)\rangle \approx N_t \frac{2}{\pi} a_1 r_m \frac{S_p(\omega_k)\; G_i(y_{ik})\; G_j(y_{jk})}{D_A} e^{i\psi_f(\omega_k, t_G)} \qquad (9.3)$$

where ψ_f, given by Eq. 8.14, is now the total phase.

SECTION X

PHASE CALIBRATION

In radio interferometry measurements, the observed phase is corrupted by unknown and unstable shifts due to instrumentation. Such phase effects can degrade the accuracy of geophysical measurements and complicate measurements of clock synchronization. Most of these instrumental effects can be removed through the use of a phase calibrator. The commonly used approach is to inject, at a point near the front of the instrumentation, a calibration signal consisting of a set of tones, equally spaced in frequency and derived from the system frequency standard. When properly applied, this technique will both correct for system phase instabilities and allow absolute clock synchronization.

To extract the calibration tones, the correlator counter-rotates the bitstream from each station with constant-frequency phaser models. The current version of the BLKII processor time-multiplexes between the tone models, dwelling for 25 msec on each. The phase of the counter-rotated tones is extracted with an arctan operation. The resulting tone phases contain all instrumental effects between the injection point and the recorder and thus can be used to remove those instrumental effects.

Two phase calibrators are currently in use: the Rogers version and the Sigman version. The Rogers phase calibrator [3] generates tones that are spaced by 1 MHz. We will assume that, when this version is used, the total mixing frequencies have been chosen so that the two tones in each 2-MHz passband have locations suitable for interpolating or extrapolating phase to other frequencies in the passband. Before interpolation, one should carry out additional calibrations to obtain an estimate for the phase-frequency slope of the tone phases so that the slope ambiguity (n x 1 μsec) due to integer-cycle ambiguities in tone phase can be removed (see Appendix G in [1]). If absolute calibration of the tone phase slope is not available, then care must be taken to see that each channel and each observation is reduced on the basis of the same ambiguity-induced slope error. Resulting BWS delay values will then all be in error by the same additive constant. In this case, clock synchronization measurements will be corrupted but geophysical/astrometric measurements will be unaffected.

When the Sigman phase calibrator is used, the tone spacing can be set to any one of a number of possible values (see Appendix B). We will assume that the selected spacing with the Sigman calibrator is 0.5 MHz and that the total mixing frequencies are chosen so that each of the four DFT frequencies (see Section VIII) for any given 2-MHz channel is nearly equal to a tone frequency. In this case, interpolation is not necessary since the tone phases are extracted at the desired frequencies. However, if clock synchronization is a goal, the a priori delay, including clock offset, still must be known well enough to resolve the ambiguity (n•2 μsec) in the "delay-resolution function" (see Section XIII).

In the following analysis, it will be assumed that phase calibrators are available at both stations and that all necessary steps have been taken to produce tone phase values at the desired passband (i.e., the DFT) frequencies.

The calibration phase at frequency ω_k within a passband is calculated as the difference in the tone phase that the correlator obtained for two stations:

$$\phi^T(\omega_k) = \Delta\phi_i{}^T(\omega_k) - \Delta\phi_j{}^T(\omega_k) \tag{10.1}$$

Based on Eq. B.8 in Appendix B, this phase is theoretically equal to

$$\phi^T(\omega_k) = \omega_k(\tau_b - \tau_c + \tau_u + \tau_I) + \phi_I + \Delta\phi_h \tag{10.2}$$

where τ_u is the station-differenced cable delay from the ϕ-cal reference point to the injection point and τ_c is the station-differenced synchronization error of the phase-cal clocks, with the differences in the order j minus i. For simplicity we have assumed that all dispersive phase shifts in ϕ_{Ik} in Eq. 5.5 occur after the tone injection points so that they appear identically in the tone and fringe phases. If significant dispersive phase shifts occur before the injection point, separate calibrations will have to be applied.

When the fringes in Eq. 9.3 have been counter-rotated with the tone phase in Eq. 10.2, the expectation value of the fringes becomes

$$\langle h''(\omega_k,t_G)\rangle \approx N_t \frac{2}{\pi} a_1 r_m \frac{S_p(\omega_k)\; G_i(y_{ik})\; G_j(y_{jk})}{D_A}\, e^{i\psi_c(\omega_k,t_G)} \tag{10.3}$$

where the corrected phase is given by

$$\psi_c(\omega_k,t_G) = \psi_f(\omega_k,t_G) - \phi^T(\omega_k) \tag{10.4}$$

Based on Eqs. 7.16, 8.14, and 10.2, the corrected phase is theoretically given by

$$\psi_c(\omega_k, t_G) = \omega_k \Delta\tau_R + \phi_B(\omega_k, t_G) + \phi_e(\omega_k, t_G) \qquad (10.5)$$

in which the residual delay is now given by

$$\begin{aligned} \Delta\tau_R = {} & \tau_{di}(t_{pi}) - \tau^u_{mi}(t_G) - \tau_{dj}(t_{pj}) + \tau^u_{mj}(t_G) \\ & + \tau_c - \tau_u + \tau_a \end{aligned} \qquad (10.6)$$

The frequencies ω_k are defined by Eq. 8.10.

The fringe phase is now theoretically free of instrumentation effects introduced between the phase-calibrator injection point and baseband.

After these corrections, the fringes are summed over a number of time points to further compress the data. If the maximum allowed amplitude loss due to incoherency is 1%, the integration interval for that sum is set by the user to a value no greater than $1/12^{th}$ the period of the highest residual fringe rate. For example, if the maximum residual fringe rate were 10 mHz, then the integration time would be 100 sec/12 ≈ 8 sec. In the following equations, it will be assumed that the loss in amplitude resulting from the sum is negligible (e.g., < 1%). Negligible phase error is introduced by this averaging. The form of the fringes is still given by Eq. 10.3 except that N_t now is equal to all of the bits summed in the integration interval and t_G refers to the center of the interval.

SECTION XI

FRINGE NORMALIZATION

This stage in the processing provides a convenient point to normalize the fringes on the basis of the number (N_t) of bits in the sum interval. The current version of Tensor provides two options: a) no normalization, which makes the fringe amplitude proportional to N_t, and b) the conventional normalization of dividing by N_t, which makes the fringe amplitude independent of N_t. The following formulation will reflect both normalization approaches.

After normalization, the fringes in Eq. 10.3 can be cast in the form

$$\langle h_c(\omega_k, t_G)\rangle = S_c c_k \, e^{i\psi_c(\omega_k, t_G)} \qquad (11.1)$$

where the phase is given by Eq. 10.5. Eqs. 5.9, 6.11 and 6.16 have been used to rewrite the amplitude in Eq. 10.3 in terms of correlated flux S_c and relative bin amplitude, which is defined by

$$c_k(t_G) \equiv \frac{2}{\pi} a_1 \, b_N(t_G) \sqrt{\frac{\kappa_i \kappa_j}{T_{si}\, T_{sj}}} \; \frac{S_p(\omega_k)\; G_i(y_{ik})\; G_j(y_{jk})}{D_A} \qquad (11.2)$$

where κ_i and κ_j are the sensitivities of the two antennas in kelvins/jansky. This formulation of the amplitude is based on the assumption that the correlated flux and antenna sensitivity are essentially constant across the (2-MHz) bandpass. The factor b_N accounts for the two possible normalization options and is given by

$$b_N = N_t \text{ for no normalization} \qquad (11.3)$$

$$= 1 \text{ for } N_t \text{ normalization} \qquad (11.4)$$

In Eq. 11.2, b_N has been made a function of t_G to account for the fact N_t might change from interval to interval as a result of lost data.

For the special case of a flat power spectrum S_p and identical bandpass shapes at the two stations, the "bandpass factor" in Eq. 11.2 can be converted through the use of Eqs. 6.12 and 8.12 to the form

$$\frac{S_p(\omega_k)\ G_i(y_{ik})\ G_j(y_{jk})}{D_A} \approx \frac{G^2(\omega_k)}{\bar{G}^2} \tag{11.5}$$

where

$$\bar{G}^2 \equiv \frac{1}{2\pi W} \int_0^\infty G^2(\omega)d\omega \tag{11.6}$$

in which doppler shifting has been neglected. For a rectangular bandpass one can readily show that the bandpass ratio in Eq. 11.5 is 1.0 so that, in this approximation, the fringes are given by

$$\langle h_c(\omega_k,t_G)\rangle = S_c\ \frac{2}{\pi}\ a_1 b_N \sqrt{\frac{\kappa_i\ \kappa_j}{T_{si}\ T_{sj}}}\ e^{i\psi_c(\omega_k,t_G)} \tag{11.7}$$

This crude form will be useful in Section XIV in defining default values for amplitude in the fringe model.

SECTION XII

CONVERSION TO COMMON GREENWICH TIME

To make all components of delay a function of "common Greenwich time," t_G, this section consolidates the time tags that characterize fringe phase. The (true) time tags t_{pi} and t_{pj} in Eq. 10.6 are related to common Greenwich time t_G through Eqs. 5.6 and 6.4, which will yield the relation

$$t_{pk} = t_G - \tau_{bk} - \tau_{Ik} \tag{12.1}$$

To convert the time tags of all quantities to t_G, expand τ_{di} and τ_{dj} in Eq. 10.6 about t_G to obtain

$$\Delta\tau_R(t_G) = \Delta\tau_g(t_G) + \Delta\tau_t(t_G) + \Delta\tau_c(t_G) - \tau_u + \tau_a + \Delta\tau_{cs} \tag{12.2}$$

in which Eqs. 6.1 and 6.20 have been used to establish the definitions for the residual geometric delay:

$$\Delta\tau_g(t_G) \equiv \frac{\hat{k}_a \bullet \left[\vec{x}_j(t_G) - \vec{x}_i(t_G)\right]}{c} - \frac{\hat{k}_m \bullet \left[\vec{x}_{mj}(t_G) - \vec{x}_{mi}(t_G)\right]}{c} \tag{12.3}$$

for the residual troposphere delay:

$$\Delta\tau_t(t_G) \equiv \tau_{tj}(t_G) - \tau_{ti}(t_G) - \tau^m_{tj}(t_G) + \tau^m_{ti}(t_G) \tag{12.4}$$

and for the residual clock offset:

$$\Delta\tau_c(t_G) \equiv \tau_{cj}(t_G) - \tau_{ci}(t_G) - \tau^m_{cj}(t_G) + \tau^m_{ci}(t_G) \tag{12.5}$$

In Eq. 12.5, the 3-lag shift in Δ_j discussed in Section VIII has been taken into account so that $\Delta_j - \Delta_i$ can be set equal to zero. The term $\Delta\tau_{cs}$ arises in the expansion about t_G and is given by

$$\Delta\tau_{cs} \equiv \dot{\tau}_{dj}(t_G)\ (\tau_{bj} + \tau_{Ij}) - \dot{\tau}_{di}(t_G)\ (\tau_{bi} + \tau_{Ii}) \qquad (12.6)$$

Thus, to apply a correction to remove this last term, one must determine the instrumental delays τ_{Ik} and the absolute bit-time errors τ_{bk} that give the offset of the sampler clocks from true time. Even if these quantities sum to 10 μsec, the correction would be less than 2 μsec/sec • 10 μsec = 20 psec. After such a correction, the only clock synchronization effect remaining in the observed delay will be the additive term $\Delta\tau_C$, the offset between phase-cal clocks at the two stations. If these time-tag corrections are carried out, the time tag of the observables can be precisely treated in subsequent modeling as though it referred to a true time of t_G at both stations. The correction would probably be applied to the overall observables for each observation (1–10 minutes), and would be computed on the basis of average delay rates for the observation (see Section XIV for a discussion of the extraction of final observables).

The fringes have been corrected for instrumental and processing effects and are theoretically given by Eq. 11.1, in which fringe phase ψ_C is given by Eq. 10.5 with residual delay $\Delta\tau_R$ given by Eq. 12.2. They will now be transformed from the RF-frequency/time domain to the BWS-delay/fringe-frequency domain where signal detection and observable extraction can be readily carried out.

SECTION XIII

TRANSFORMING TO THE BWS-DELAY AND FRINGE-FREQUENCY DOMAINS

When an accurate correlator model is used, the counter-rotated fringe phase in Eq. 10.5 is nearly a linear function of both time and frequency. Thus, if the frequency slope (i.e., residual BWS delay) and time slope (i.e., residual fringe frequency) were relatively accurately known, the fringes could be counter-rotated over both dimensions with a linear phase model and coherently summed over time and frequency. Those slopes, however, are generally not known accurately enough to perform a coherent sum. Thus, counter-rotation for a range of "trial" slopes is carried out by means of an FFT over frequency and an FFT over time. These FFTs transform the fringes from the RF-frequency/time domain to the BWS-delay/ fringe-frequency domain. For output points (slopes) near the actual BWS delay and fringe-frequency, the fringes will coherently sum to form a peak in output amplitude that will allow detection and observable extraction. Appendix D and Figures 5a and 5b outline the transformations in terms of data structure.

To carry out these transformations, the fringes in Eq. 11.1 are counter-rotated by two consecutive FFTs as follows:

$$R'(\tau_f,\omega_f) = \sum_{k,t_G} h_c(\omega_k,t_G)\, e^{-i\omega_k''\tau_f}\, e^{-i\omega_f t_G''} \tag{13.1}$$

where, for standard fast Fourier transforms, the time and frequency variables are both zero for the first point:

$$\omega_k'' = \omega_k - \omega_1 \tag{13.2}$$

$$t_G'' = t_G - t_1 \tag{13.3}$$

where ω_1 and t_1 are the values for the first frequency and time, respectively.

The sum over frequency is normally performed over the bins from all channels in a band (e.g., S or X), while the sum interval over time is selected by the user. For a standard FFT, the "trial" values for (BWS) delay τ_f and fringe frequency ω_f are given by

$$\tau_f = n_\tau \Delta\tau_f \qquad n_\tau = 0,1,2\ldots N_\tau \tag{13.4}$$

$$\omega_f = n_\omega \Delta\omega_f \qquad n_\omega = 0,1,2\ldots N_\omega \tag{13.5}$$

where $\Delta\tau_f$ ($\Delta\omega_f$) is the separation between the delay (fringe-frequency) points. (Negative "trial" values of BWS-delay and fringe frequency reside in the upper half of a standard FFT output, as noted in Appendix D.) As illustrated in Appendix D, the separation for the BWS-delay coordinate is of approximately 1/4 to 1/2 the inverse of the RF spanned bandwidth while the bin width in the frequency direction is approximately 1/4 to 1/2 the inverse of the integration time.

Because the bin spacing is 0.5 MHz in RF frequency, the FFT output is cyclic as a function of BWS delay, with a cycle interval of 2 μsec. Thus, to obtain absolute delay measurements, the a priori error on the calibrated delay must be no greater than 1 μsec. Typically, a priori errors due to geometric, tropospheric and ionospheric delays will not be large enough to prevent resolution of this n•2 μsec ambiguity. The offset between station clocks, however, can potentially be a large unknown value. In this situation, a relatively accurate estimate of residual delay can be obtained from the single-channel delay obtained directly from the lag-domain fringes generated by a strong source. This offset, however, must first be corrected for the instrumental offsets τ_I and τ_b. With stable clocks, analysis of a single observation in this manner should usually be adequate to determine the absolute clock offset and thereby allow removal of the n•2 μsec ambiguities for a whole session.

As illustrated in Figs. 5a and 5b, the FFT over RF frequency is carried out first. To reduce memory and computation requirements, only a subset of resulting BWS delay points, selected on the basis of the a priori delay, are retained to be transformed over time (see Appendix D).

To compensate for the two origin offsets in Eq. 13.2 and 13.3, the output of the FFTs is counter-rotated at each point as follows:

$$R(\tau_f,\omega_f) = e^{i[(\omega_z-\omega_1)\tau_f+(t_z-t_1)\omega_f]}\; R'(\tau_f,\omega_f) \qquad (13.6)$$

This counter-rotation places the "origin" of the FFT frequency variable at a reference frequency ω_z and the "origin" of the FFT time variable at the reference time t_z. Both reference values can be specified by the user but should be computed according to the expressions in Appendix C. Both values are analytically enforced by the counter-rotation in Eq. 13.6 and by the least-squares model explained in the next section. Based on Eqs. 10.5, 11.1, 13.1, and 13.6, the expectation value of the resulting fringes is given by

$$\langle R(\tau_f,\omega_f)\rangle = \sum_{k,t_G} S_c c_k \; e^{i\left[\omega_k\Delta\tau_R+\phi_B+\phi_e-(\omega_k-\omega_z)\tau_f-(t_G-t_z)\omega_f\right]} \qquad (13.7)$$

where $\Delta\tau_R$ is given by Eq. 12.2, and c_k is given by Eq. 11.2.

This fringe function peaks in amplitude at the values for τ_f and ω_f that are closest to the actual BWS delay and delay rate, as illustrated in the next section. For stable instrumentation, the shape of the fringe function is a sinx/x form along the fringe-frequency axis. Along the BWS-delay axis, the fringe function has a main lobe centered on the true delay with a sidelobe structure dependent on the placement of channels within the spanned bandwidth, relative amplitude of the channel fringes, and the coherence between channels.

For the transformation approach outlined above, amplitude can be lost if a priori values for baseline and source position are very inaccurate. Since the residual fringe frequency in the passed fringes scales with channel frequency, each channel will have a different fringe frequency. Thus, in the double FFT over time and RF frequency, the output of the time FFT will not be perfectly coherent when summed across channels. The smaller the residual delay rate, the smaller the amplitude loss due to this effect will be. A limit can be placed on such amplitude loss by adjusting the integration time (T_I) so that the change of residual fringe frequency across channels is considerably less than the width ($2/T_I$) of the main lobe of the FFT's frequency filter. As an example, the following approximate formula for the maximum integration time applies when the BWS channels are uniformly spaced across the RF band:

$$T_{max} \approx \frac{2.5 \sqrt{\varepsilon_A}}{\Delta f_s \; \Delta\dot{\tau}_\phi} \tag{13.8}$$

where ε_A is the maximum fractional decrease (e.g., 0.01) in amplitude to be allowed, Δf_s is the spanned bandwidth, and $\Delta\dot{\tau}_\phi$ is the maximum expected residual delay rate. Other distributions of channels across the RF band may have significantly different values for maximum integration time.

To illustrate the limits set by Eq. 13.8, let the desired integration time be 1000 sec, the approximate limit set by the instability of the current frequency standards. For a spanned bandwidth of 400 MHz and a maximum amplitude loss of 10%, Eq. 13.8 would limit the residual delay rate to about 2 psec/sec or less. A delay rate error of 2 psec/sec corresponds to a baseline error of about 8 m and a source position error of about 0.2 arcseconds (for a 9000-km baseline). These loose requirements on the a priori delay will almost always be satisfied if the baseline and source have been previously measured by the VLBI technique. In the occasional cases for which the source or baseline is being accurately measured for the first time, preliminary "calibration" observations may be necessary (e.g., by "packing" the channels side-by-side for a few observations or observing the source first on a shorter baseline). As VLBI matures, a smaller and smaller fraction of sources and baselines will have poor a priori delays.

These accuracy requirements for a priori baseline and source positions are based on a uniform distribution of channels across the spanned bandwidth. As another example, one can use the channel frequency values listed in Appendix E, which are closer to the distributions used to optimize delay measurements. For this distribution, the limits on a priori that are presented above must be tightened by about a factor of 1.3.

The amplitude loss in Tensor discussed above occurs when the a priori delay model is very poor. Since special methods can be employed to treat such cases, the only impact of this limitation is the extra effort that might be required the first time an inaccurate baseline or source position is used. Plans have been formulated for correcting this limitation in Tensor, thereby increasing the allowed range of uncertainty for the a priori delay model.

SECTION XIV

OBSERVABLE EXTRACTION

The first step in extracting information from the fringes produced by the operation in Eq. 13.6 is to find the maximum amplitude (RSS of real and imaginary parts) as a function of BWS delay (τ_f) and fringe frequency (ω_f). A priori information can be used to restrict the range over which the search for the maximum is carried out. Since the fringes that are input to the FFT have a frequency spacing of 0.5 MHz, the output fringes will repeat every 2 μsec as a function of BWS delay. The a priori information should be accurate enough to prevent this n•2 μsec ambiguity. Even if the a priori error in delay is too large (> 1 μsec) due to clock error, the uncertainty in the other components in the delay will usually be accurate enough to select a common (but arbitrary) ambiguity for all observations. In subsequent multiparameter fits, this compromise will not degrade estimates of geophysical and astrometric parameters, but will, of course, prevent synchronization of station clocks.

The FFT output point at which the maximum amplitude occurs will be called the peak point. Data in the vicinity of the peak point are fit by least-squares to extract the fringe observables. Only fringe values within 1 to 3 intervals of the peak point (9 to 49 points in all) are included in the fit. The model for the fringes in the least-squares analysis is given by

$$R_m(\tau_f,\omega_f) = A_s\, e^{i\phi_s} \sum_{k,t_G} c_{mk}\, e^{i\left[(\omega_k-\omega_z)(\tau_s-\tau_f)+(t_G-t_z)(\omega_k\dot{\tau}_{\phi s}-\omega_f)\right]} \tag{14.1}$$

where t_z, ω_z are the reference time and frequency used in Eq. 13.6. The four solve-for parameters are amplitude A_s, BWS delay τ_s, RF phase ϕ_s, and phase-delay rate $\dot{\tau}_{\phi s}$.

Model values for the relative amplitudes c_{mk} can currently be specified in two ways. In the default mode, they are automatically set equal to a crude value that is valid for a system in which all channels are identical (e.g., have the same correlated flux, the same rectangular 2-MHz-wide bandpass function, the same antenna sensitivity, and the same system temperature). That default value is given by

$$c_{mk} = \frac{2}{\pi}\, a_1 \tag{14.2}$$

As one can see by comparing the default value with the amplitude in Eq. 11.7, the default amplitudes have been selected so that the estimated fringe amplitude in the default mode will be approximately given by

$$A_s \approx S_c \, b_N \sqrt{\frac{\kappa_i \kappa_j}{T_{si} T_{sj}}} \qquad (14.3)$$

where the temperatures are the common temperature for all channels. When accurate delay and amplitude measurements are the goal, one has the second, more accurate option of supplying to the post-Tensor software numerical values for the relative amplitudes. With this option the user has the maximum flexibility in modeling the fringe amplitudes, regardless of his approach for obtaining them. One approach is to measure the quantities necessary to evaluate the theoretical expression for amplitude in Eq. 11.1. For example, if the correlated flux is the same for all channels across the spanned bandwidth, the relative amplitudes are theoretically given by Eq. 11.2, which requires estimates for bandpass shapes, system temperatures and antenna sensitivities for each channel. (In very accurate applications, it may be necessary to upgrade Eq. 11.2 to account for intrachannel errors in relative bin amplitude that were introduced by the limited-lag transform but neglected after Section VIII.) Under these assumptions, the estimated amplitude will be equal to the correlated flux ($A_S = S_C$). An alternate, less theoretical approach for estimating relative bin amplitudes is to separately extract the bin amplitudes for a strong source with constant correlated flux across the spanned bandwidth, and to use their relative magnitudes along with a scaling factor to compute the values for c_{mk}. An error in the scaling factor will cause a scale error in the estimated fringe amplitude A_S but will not degrade the estimate of BWS delay, delay rate, and phase. If the correlated flux of the strong source is known, the scaling factor can also be obtained from the calibration run.

If accurate values for relative bin amplitude are supplied and if the observed fringes are sufficiently coherent over frequency channels, one can show (Appendix C) that a best fit will be obtained when the model phase (phase in Eq. 14.1) is adjusted so that it approximates (in a least-square sense) the actual phase (the phase in Eq. 13.7):

$$\begin{aligned}(\omega_k - \omega_z)(\tau_s - \tau_f) + (t_G - t_z)(\omega_k \dot{\tau}_{\phi s} - \omega_f) + \phi_s \approx \\ \omega_k \Delta\tau_R(t_G) + \phi_B(\omega_k, t_G) + \phi_e(\omega_k, t_G) - (\omega_k - \omega_z)\, \tau_f \\ - (t_G - t_z)\, \omega_f + 2n\pi \end{aligned} \qquad (14.4)$$

where $2n\pi$ represents the integer-cycle ambiguity in fringe phase and where $\Delta\tau_R(t_G)$ is given by Eq. 12.2. If one cancels like terms on either side and expands the structure phase ϕ_B about (ω_z, t_z) and $\Delta\tau_R$ about t_z, this equation can be rewritten as

$$\phi_s + (\omega_k - \omega_z)\,\tau_s + (t_G - t_z)\,\omega_k\,\dot{\tau}_{\phi s} \approx$$

$$\omega_z \Delta\tau_R(t_z) + (\omega_k - \omega_z)\,\Delta\tau_R(t_z) + (t_G - t_z)\,\omega_k\,\Delta\dot{\tau}_R(t_z)$$

$$+ \phi_B(\omega_z,t_z) + (\omega_k - \omega_z)\,\frac{\partial\phi_B(\omega_z,t_z)}{\partial\omega} + (t_G - t_z)\,\frac{\partial\phi_B(\omega_z,t_z)}{\partial t}$$

$$+ \frac{k_e\,\Delta N_e(t_z)}{\omega_k} \tag{14.5}$$

where the last term is the ionosphere phase ϕ_e expressed in terms of frequency and differential electron content $\Delta N_e(t)$. Theoretical expressions for the three estimated parameters can be obtained by substituting the right-hand-side of this equation (which is the expansion of Eq. C.14 in Appendix C) in place of ψ_c in Eqs. C.19, C.20 and C.21, which yields the following approximate expressions for BWS delay, phase-delay rate and phase-delay:

$$\hat{\tau}_s \approx \Delta\tau_R(t_z) + \frac{\partial\phi_B(\omega_z,t_z)}{\partial\omega} - \frac{k_e\overline{\Delta N_e}}{\omega_\tau^2} \tag{14.6}$$

$$\hat{\dot{\tau}}_{\phi s} \approx \Delta\dot{\tau}_R(t_z) + \frac{1}{\omega_z}\,\frac{\partial\phi_B}{\partial t} + \frac{k_e\overline{\Delta\dot{N}_e}}{\omega_{\dot{\tau}}^2} \tag{14.7}$$

$$\hat{\tau}_{\phi s} \equiv \hat{\phi}_s/\omega_z \tag{14.8}$$

$$\approx \Delta\tau_R(t_z) + \frac{1}{\omega_z}\,\phi_B(\omega_z,t_z) + \frac{k_e\overline{\Delta N_e}}{\omega_z\omega_\phi} + \frac{2n\pi}{\omega_z} \tag{14.9}$$

where ω_τ, $\omega_{\dot\tau}$, and ω_ϕ are effective frequencies to be used for for computation of the ionosphere effect and $\overline{\Delta N_e}$ and $\dot{\Delta N_e}$ are computed on the basis of electron content. Expressions for $\overline{\Delta N_e}$, $\dot{\Delta N_e}$ and the three effective frequencies are derived in Appendix E. Residual delay $\Delta\tau_R$ is given theoretically by Eq. 12.2, but evaluated at reference time t_z.

In most applications, the model fringes in Eq. 14.1 should be carefully constructed. When accurate estimates of BWS delay are required, for example, the relative magnitudes of the bin amplitudes c_{mk} should be accurately specified so that the shape of the "delay resolution function" closely matches the actual shape. The use of the accurate relative bin amplitude also simplifies the problem of computing effective frequencies for dual-band ionosphere calibrations, as explained in Appendix E.

Another important consideration in assessing the accuracy of the fringe model is the phase coherence of the observed fringes. Since phase coherence was an important goal when the station instrumentation was designed and developed, the fringe model in Eq. 14.1 has been based on the assumption that the instrumental contribution to fringe phase is coherent (i.e., perfectly linear) as a function of time and RF frequency. It is likely, however, that the actual level of coherence will not be adequate in some applications. Given a strong source, a test of coherence can be carried out by extracting the fringe phase at each time point (e.g., each second) and for each frequency bin for each channel and then fitting all of those phase values with a phase model that is linear in time and frequency (e.g., as in Eq. 14.1). Plots of the residuals will reveal nonlinear trends as a function of time and frequency. Incoherence over time usually cannot be modeled and corrected since it is typically a consequence of instability in the frequency standards. Incoherence over frequency, on the other hand, is likely to consist of the same nonlinear pattern from source to source. If that is the case, bin-specific phase corrections can be computed on the basis of the aforementioned "coherence residuals" across frequency and added to the phase of the model fringes. Such a correction would make the shape of the model "delay resolution function" more accurately represent the actual shape and would lead to more accurate estimates of BWS delay.

An example of a fit to Tensor output is shown in Figures 7a and 7b. These data, which were reduced by T.G. Lockhart using his post-Tensor software, were obtained on an OVRO/Mojave baseline for the source 3C84. Before the Tensor FFT's, the data in the time and channel-frequency domains consisted of 30 time points spaced by 2 seconds and 8 upper-sideband channels with L.O. frequencies of +(0, 10, 40, 100, 210, 290, 340, 360) MHz relative to 8210.99 MHz. A 2048-point FFT over channel frequency, followed by a 64-point FFT over time, produced the data points shown in Figures 7a and 7b. To reduce data volume, only two slices of the full two dimensions are presented. The slices

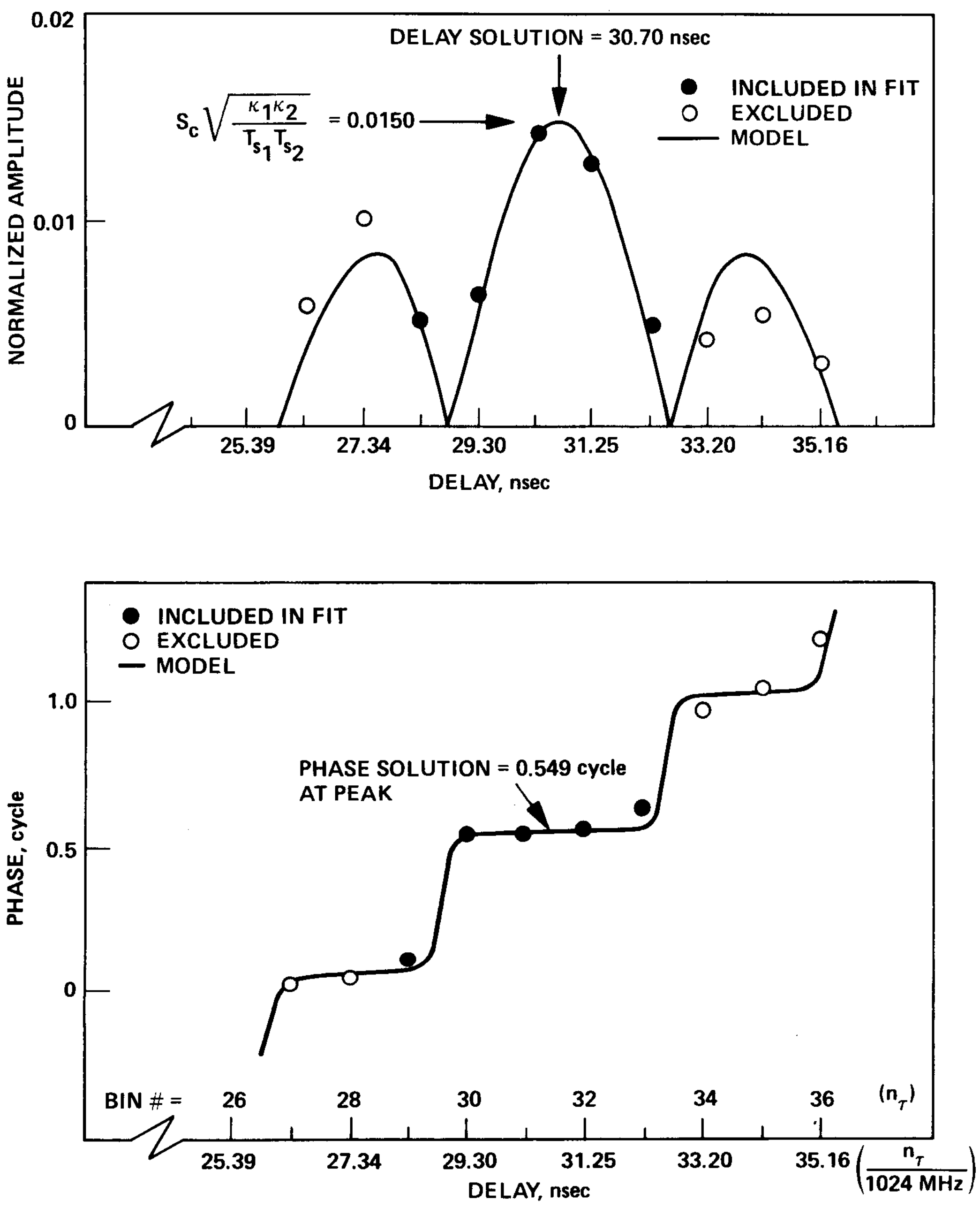

Figure 7a. Example of Tensor Output: Amplitude and Phase vs. Delay

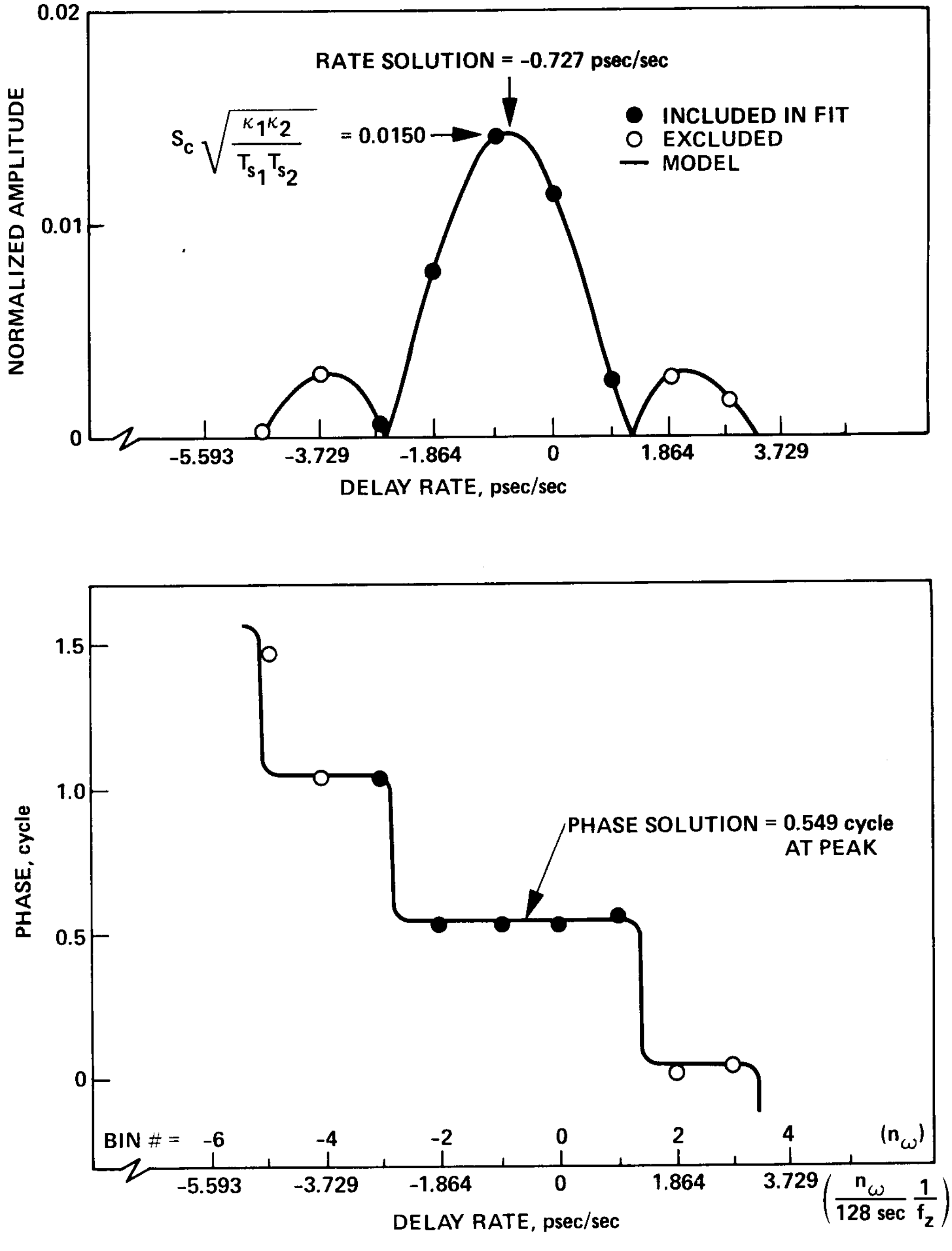

Figure 7b. Example of Tensor Output: Amplitude and Phase vs. Delay Rate

pass through peak amplitude along the delay axis and along the delay rate axis. Note that the amplitude has been normalized to correspond with the "units" of estimated amplitude, A_s, in Eq. 14.3, with $b_n = 1$. The solid curves in the figures represent the fit function given in Eq. 14.1. A reference frequency of f_z = 8380.74 MHz was used in the fit. The sharp 1/2 cycle changes in phase vs. delay and delay rate are due to abrupt changes in quadrants when the amplitude becomes very small. The fit as a function of delay rate is very good for both amplitude and phase. On the other hand, the fit as a function of delay is fairly good in the main lobe, but deviates considerably in the sidelobes. These deviations, which should be eliminated by improvements in hardware and/or better modeling, are probably due to non-linear variations of fringe phase across frequency channels or by unmodeled variations in fringe amplitude across frequency channels.

SECTION XV

MODEL RESTORATION

After the (residual) observables have been extracted by the least-squares fit, the post-Tensor software computes a model delay (or delay rate) based on the processor model and adds this model delay (or delay rate) to the estimated observables in order to form total observables free of processor modeling.

Two approaches were considered for computing the restored model: analytical recomputation of the correlator model for each delay component (i.e., geometric, tropospheric, and clock) or interpolation between the actual numerical delay values used by the correlator. Since analytical recomputation of the processor models is prone to error and inconsistency, the numerical approach was selected. The correlator passes for each station an array of values for the total delays τ_{mi}, τ_{mj} used to calculate the quantized bitstream offsets. These array values, which the correlator computed on the basis of Eq. 6.2, are separated by 2-4 seconds. The post-Tensor software interpolates between the passed values to obtain model values at desired times.

Were it not for the "retarded baseline" ("transit time") complication in the geometric component, the interpolated model delay values could simply be differenced between stations and added to the residual delay. For geophysical/astrometric applications, however, the post-Tensor software must restore the model in a form that will lead to a geometric component that is based on the definition commonly assumed in subsequent multi-parameter fitting software: a wavefront arriving at antenna i at true time t will reach antenna j at true time $t + \tau_g(t)$, where $\tau_g(t)$ is defined to be the geometric delay at true time t. This definition of the geometric delay incorporates the effect of the motion of station j during wave transit, an effect that is not present in the straight difference between stations.

The preceding definition can easily be converted to an equation for computing geometric delay in terms of station locations and source direction. The phase of the incoming signal is given in terms of the wave vector $\vec{k}$ and frequency ω by the exponent in Eq. 5.1. Let $\vec{x}_i(t)$ and $\vec{x}_j(t)$ represent the positions of the two antennas as a function of true time. The phase arriving at antenna i at time t will reach antenna j at time $t + \tau_g$ when the following phase relation is satisfied:

$$\vec{k} \bullet \vec{x}_i(t) - \omega t = \vec{k} \bullet \vec{x}_j(t + \tau_g) - \omega(t + \tau_g) \qquad (15.1)$$

Rearrangement of terms produces an expression for τ_g:

$$\tau_g(t) = \frac{\hat{k}}{c} \bullet \left[\vec{x}_j(t + \tau_g) - \vec{x}_i(t)\right] \qquad (15.2)$$

where $\hat{k}$ is the unit vector in the direction of $\vec{k}$. The difference in station locations in brackets is equal to the baseline vector between stations except for the small offset by τ_g in the argument of $\vec{x}_j$. This argument offset is the origin of the term "retarded baseline" correction.

To illustrate the magnitude of the retarded-baseline correction, expand $\vec{x}_j(t)$ about t:

$$\vec{x}_j(t + \tau_g) \approx \vec{x}_j(t) + \dot{\vec{x}}_j \, \tau_g \qquad (15.3)$$

in which higher order terms have been neglected. For geometric delays less than 0.03 sec, the higher order terms contribute less than

$$\Delta\tau_g \lesssim \frac{1}{2c} \, |\ddot{\vec{x}}_j| \tau_g^2 \qquad (15.4)$$

$$\lesssim 0.1 \text{ psec} \qquad (15.5)$$

which is negligibly small. Thus, the magnitude of the retarded-baseline correction is bounded by

$$\Delta\tau_g \lesssim \frac{1}{c} \, |\dot{\vec{x}}_j| \tau_g \qquad (15.6)$$

$$\lesssim 3 \times 10^{-6} * 0.03 \text{ sec} \qquad (15.7)$$

$$\lesssim 90 \text{ nsec} \qquad (15.8)$$

for intercontinental baselines. Since this effect is relatively small, relatively inaccurate estimates for source positions and baseline vector provide accurate estimates for this correction. For example, a 100-m error in baseline vector or a 2 arcsecond error in source position will result in an error of less than 0.1 cm in the correction. Thus, the retarded-baseline effect can be accurately introduced in the final observable so that the conventional definition of geometric delay will apply to the geometric component of the total delay.

The expression for geometric delay can be cast into a more practical form by replacing τ_g on the right-hand side of Eq. 15.3 by the symmetric geometric "delay"

$$\tau_g^s(t) \equiv \frac{\hat{k}}{c} \bullet \left[\vec{x}_j(t) - \vec{x}_i(t)\right] \tag{15.9}$$

Since the retarded baseline effect is less than 30 m, this substitution results in errors less than 0.2 psec. When Eq. 15.3 is combined with Eq. 15.2, the geometric delay becomes

$$\tau_g(t) \approx \tau_g^s(t) + \Delta\tau_g^R(t) \tag{15.10}$$

where the symmetric geometric "delay" τ_g^s is given by Eq. 15.9 and the transit-time correction by

$$\tau_g^R(t) \equiv \frac{\hat{k}}{c} \bullet \left[\vec{x}_j(t) - \vec{x}_i(t)\right] \frac{\hat{k}\bullet\dot{\vec{x}}_j}{c} \tag{15.11}$$

In order to produce observables satisfactory for both source structure and geophysical/astrometric applications, the model delay is restored in two steps. The first step restores a model delay whose geometric component is of the form of Eq. 15.9. This leads to total observables that are symmetric with respect to interchange of stations, as required by source structure work. The second step adds a transit-time correction of the form of Eq. 15.11, which produces total observables based on the conventional definition of geometric delay, as assumed in geophysical/astrometric applications.

In the first step, the restored model is computed as

$$\tau_{mA}(t_z) = \tau_{mi}^u(t_z) - \tau_{mj}^u(t_z) \tag{15.12}$$

in which the unretarded model delays are obtained by interpolating between the numerical values passed by the correlator. Total observables, essentially free of correlator modeling, are obtained by adding the numerically interpolated models to the residual observables produced by least-squares analysis:

$$\tau_{BWS}^{(1)}(t_z) = \hat{\tau}_s + \tau_{mA}(t_z) \tag{15.13}$$

$$\dot{\tau}_{\phi}^{(1)}(t_z) = \hat{\dot{\tau}}_{\phi s} + \dot{\tau}_{mA}(t_z) \tag{15.14}$$

$$\tau_{\phi}^{(1)}(t_z) = \hat{\tau}_{\phi s} + \tau_{mA}(t_z) \tag{15.15}$$

where $\dot{\tau}_{mA}$ is the numerically computed time derivative of τ_{mA}.

One can obtain a theoretical expression for the total observables of step 1 by combining the theoretical forms for the observables in Eq. 15.13 to 15.15 with the theoretical expression for the residual delay obtained from Eqs. 12.2 to 12.5 and Eqs. 14.6 to 14.9:

$$\tau_{BWS}^{(1)} = \tau_R^{(1)}(t_z) + \frac{\partial\phi_B(\omega_z,t_z)}{\partial\omega} - \frac{k_e\overline{\Delta N_e}}{\omega_\tau^2} \tag{15.16}$$

$$\dot{\tau}_{\phi}^{(1)} = \dot{\tau}_R^{(1)}(t_z) + \frac{1}{\omega_z}\frac{\partial\phi_B(\omega_z,t_z)}{\partial t} + \frac{k_e\overline{\Delta\dot{N}_e}}{\omega_{\dot{\tau}}^2} \tag{15.17}$$

$$\tau_{\phi}^{(1)} = \tau_R^{(1)}(t_z) + \frac{1}{\omega_z}\phi_B(\omega_z,t_z) + \frac{k_e\overline{\Delta N_e}}{\omega_z\,\omega_\phi} + \frac{2n\pi}{\omega_z} \tag{15.18}$$

where

$$\tau_R^{(1)}(t_z) = \tau_g^s(t_z) + \tau_t(t_z) + \tau_c(t_z) - \tau_u + \tau_a + \Delta\tau_{cs} \tag{15.19}$$

in which τ_g^s is the actual (symmetric) geometric delay given by Eq. 15.9 with $\hat{k} = \hat{k}_a$, and where τ_t and τ_c are the differences between stations of the total actual troposphere and clock terms, respectively, in the order j minus i. These total observables are passed to source-structure software for further processing.

The second step in model restoration produces observables suitable for geophysical/astrometric applications. In this step, a model delay that accurately approximates the transit-time correction in Eq. 15.11 is added to the observables computed in step 1 (Eqs. 15.13, 15.14, and 15.15). As indicated earlier in this section, a relatively inaccurate model for source position and station location will not significantly degrade final delay accuracy. The resulting observables, which will be denoted by a superscript$^{(2)}$, are still given theoretically by Eqs. 15.16, 15.17, and 15.18, except that $\tau_R^{(1)}$ becomes

$$\tau_R^{(2)} = \tau_g(t_z) + \tau_t(t_z) + \tau_c(t_z) - \tau_u + \tau_a + \Delta\tau_{cs} \qquad (15.20)$$

where $\tau_g(t_z)$ is now the actual geometric delay based on the conventional definition, as in Eqs. 15.2 or 15.10.

As shown by Eqs. 15.16, 15.17 and 15.18, the total observables are a sum of terms due to geometry, troposphere, clock, charged particles, source structure, and three "instrumental" effects. When absolute clock synchronization is a goal, postprocessor software will apply corrections to remove the phase-cal cable delay τ_u and the "antenna" delay τ_a. In future ultraprecise applications, the time-tag term $\Delta\tau_{cs}$ and the source-structure terms involving ϕ_B might be removed also. After these corrections have all been applied, the final three observables (BWS delay, phase-delay rate, and phase delay) are each a sum of terms due to geometry, troposphere, charged particles, and clock offsets, where all terms can be modeled as though they were observed at true time t_z. As mentioned in Section V, the geometric delay is modeled relative to the effective positions (intersection of axes) of the two antennas. This set of observables is extracted for each RF band.

SECTION XVI

SUMMARY

This report has presented radio interferometry theory as it applies to the BLKII processor, including many detailed instrumental and processing effects that are important in source-structure and geophysical/astrometric measurements. The analysis has covered all major data reduction steps from signal reception to the output observables of amplitude, BWS delay, phase delay and phase-delay rate. Even though the BLKII processor is vastly superior to its predecessor in a number of ways, a number of additional improvements are being considered, as noted in the introduction. We plan to implement many of these improvements as resources permit.

SECTION XVII

REFERENCES

1. Thomas, J. B., "An Analysis of Radio Interferometry with the Block 0 System," JPL Publication 81-49, Jet Propulsion Laboratory, Pasadena, California, Dec. 1981.

2. Rogers, A. E. E., and Clark, T. A., "Mark III Data Acquisition Terminal," Crustal Dynamics Project, Goddard Space Flight Center, Greenbelt, Maryland, Jan. 1982.

3. Rogers, A. E. E., "A Receiver Phase and Group Delay Calibrator for Use in Very Long Baseline Interferometry," Haystack Observatory Technical Note 1975-6.

4. Rogers, A. E. E., "Very-Long-Baseline Interferometry with Large Effective Bandwidth for Phase-Delay Measurements," Radio Science, 5, p. 1239, 1970.

5. Fanselow, J. L., "Observation Model and Parameter Partials for the JPL VLBI Parameter Estimation Software 'MASTERFIT-V1.0'," JPL Publication 83-39, Jet Propulsion Laboratory, Pasadena, California, Dec. 1983.

6. van Vleck, J. H., and Middleton, D., "The Spectrum of Clipped Noise," Proc. IEEE, Vol. 54, No. 1, 1966.

7. Thomas, J. B., "An Analysis of Source Structure Effects in Radio Interferometry Measurements," JPL Publication 80-84, Jet Propulsion Laboratory, Pasadena, California, Dec. 1980.

APPENDIX A

A COMPLETE DERIVATION OF THE CROSS-CORRELATION FUNCTION

This appendix presents a complete derivation of the cross-correlation function, taking into account the statistics and the spatial distribution of the emissions of the natural source.

The radio noise generated by a very distant extended natural source can be expressed as a superposition of plane waves in the form

$$E(\vec{x},t) = \int_{\hat{k}} \int_{0}^{\infty} A(\hat{k},\omega)\, e^{i\omega[t-\hat{k}\cdot\vec{x}/c]}\, d\omega d\Omega + c.c. \qquad (A.1)$$

where $E(\vec{x},t)$ is the electric field at position $\vec{x}$ and true time t. For simplicity, the electric field is assumed to be linearly polarized. The function $A(k,\vec{x})$ is the Fourier amplitude at frequency ω for the wave received from direction $\hat{k}$, while c.c. denotes the complex conjugate. As in Section V, all quantities are measured with respect to a geocentric frame. The wave direction $\hat{k}$ can be expressed as a function of two parameters and, in the case of right ascension (r.a.) and declination, becomes

$$\hat{k} = -\,(\cos\delta\,\cos\alpha,\ \cos\delta\,\sin\alpha,\ \sin\delta) \qquad (A.2)$$

where α, δ are the apparent right ascension and declination relative to the true equatorial coordinates of date. The quantity $d\Omega$ represents a differential solid angle such as $\cos\delta\ d\alpha\ d\delta$ in the case of right ascension and declination. In the following steps, we will use the wave vector $\vec{k} = \omega\hat{k}/c$.

The electric field detected at antenna j is given by

$$E_j(t) = E(\vec{x}_j(t),t) = \int_{\hat{k}} \int_{0}^{\infty} A(\hat{k},\omega)\, e^{i[\omega t-\vec{k}\cdot\vec{x}_j(t)]}\, d\omega d\Omega + c.c. \qquad (A.3)$$

where $\vec{x}_j(t)$ is the position of antenna j as a function of true time. (See Section V for a definition of antenna location.) This signal will be received by the antenna and passed through various filters and mixers. The modeling of the composite effect of instrumentation is discussed in Section V. Following that derivation, the signal component due to the natural source can be written in the form

$$V_j^q(t_{bj}) = \int_{\hat{k}} \int_0^{\infty} A(\hat{k},\omega) G_j(y_j) \; e^{i[\omega t_{pj} - \vec{k}\cdot\vec{x}_j(t_{pj}) - \alpha_{Ij}(\omega, t_{pj})} d\omega d\Omega$$

$$+ \text{ c.c.} \tag{A.4}$$

where the doppler-shifted passband argument is given by

$$y_j = \omega \; (1 - \hat{k} \cdot \dot{\vec{x}}_j/c) \tag{A.5}$$

and where instrumental phase terms are given by

$$\alpha_{Ij}(\omega, t_{pj}) \equiv \omega_{hj} \; t_{pj} + \phi_{hj} + \omega\tau_{aj} + \phi_{Ij}(y_j) \tag{A.6}$$

As in the text, t_{pj} is the true time that corresponds to bit time t_{bj}. (See Eq. 5.6.)

We will first compute the expectation of the product of two analog signals as described by Eq. A.4 and then compute the normalization. The expectation value of the voltage product is given by

$$\left\langle V_i^q(\hat{t}_{bi}) \; V_j^q(\hat{t}_{bj}) \right\rangle =$$

$$\int_{\hat{k}'} \int_0^{\infty} \int_{\hat{k}} \int_0^{\infty} A(\hat{k},\omega) A^*(\hat{k}',\omega') \; G_i(y_i) \; G_j(y_j') \; e^{i\psi} \; d\omega \; d\Omega \; d\omega' \; d\Omega'$$

$$+ \int_{\hat{k}'} \int_0^{\infty} \int_{\hat{k}} \int_0^{\infty} A(\hat{k},\omega) \; A(\hat{k}',\omega') \; G_i(y_i) \; G_j(y_j') \; e^{i\psi b} \; d\omega \; d\Omega \; d\omega' \; d\Omega'$$

$$+ \text{ c.c.} \tag{A.7}$$

where

$$y_j' = \omega' \; (1 - \hat{k}' \cdot \dot{\vec{x}}_j/c) \tag{A.8}$$

$$\psi = \omega\hat{t}_{pi} - \vec{k} \cdot \vec{x}_i(\hat{t}_{pi}) - \omega'\hat{t}_{pj} + \hat{k}' \cdot \vec{x}_j(\hat{t}_{pj})$$
$$- \alpha_{Ii}(\omega, \hat{t}_{pi}) + \alpha_{Ij}(\omega', \hat{t}_{pj}) \tag{A.9}$$

and ψ_b is a similar expression that will not be needed. The quantities t_{pk} are the offset values for the true time corresponding to t_{bk}, as in Eqs. 6.8 and 6.9 in the text (i.e., $\hat{t}_{bj} = t_{bj} + \Delta$ implies $\hat{t}_{pj} = t_{pj} + \Delta$).

We will assume that the natural source is completely incoherent, which means

$$\langle A(\hat{k},\omega)\ A^*(\hat{k}',\omega')\rangle = \frac{1}{2}\ S_p(\hat{k},\omega)\ \delta(\hat{k} - \hat{k}')\ \delta(\omega - \omega') \qquad \text{(A.10)}$$

where $S_p(\hat{k},\omega)$ is the power spectrum for direction $\hat{k}$ and $\delta(z)$ is a Dirac delta function.* That is, emissions from different areas of the source are uncorrelated. Furthermore, the noise emitted by a given area is stationary and therefore possesses uncorrelated frequency components. Since the signal is real, we know

$$A(\hat{k},\omega) = A^*(\hat{k}, -\omega) \qquad \text{(A.11)}$$

This relation and Eq. A.10 give

$$\langle A(\hat{k},\omega)\ A(\hat{k}',\omega')\rangle = \frac{1}{2}\ S_p(\hat{k},\omega)\ \delta(\hat{k} - \hat{k}')\ \delta(\omega + \omega') \qquad \text{(A.12)}$$

$$= 0 \text{ for } \omega \text{ and } \omega' > 0 \qquad \text{(A.13)}$$

Under these assumptions, Eq. A.7 becomes

$$\langle v_i^q(\hat{t}_{bi})\ v_j^q(\hat{t}_{bj})\rangle = \frac{1}{2} \int_{\hat{k}} \int_0^\infty S_p(\hat{k},\omega)\ G_i(y_i)\ G_j(y_j)\ e^{i\psi_I} d\omega d\Omega$$
$$+ \text{ c.c.} \qquad \text{(A.14)}$$

where

$$y_n = \omega\ (1 - \hat{k} \bullet \dot{\vec{x}}_n/c) \qquad n = i \text{ or } j \qquad \text{(A.15)}$$

---

*For two particular direction parameters (β, γ), the $\delta(\hat{k} - \hat{k}')$ delta function denotes $\delta(\beta - \beta')\ \delta(\gamma - \gamma')$. Furthermore, we will require β and γ to satisfy the relation $d\beta\ d\gamma = d\Omega$.

$$\psi_I = \omega\ (\hat{t}_{pi} - \hat{t}_{pj}) + \vec{k} \bullet \vec{B}_r - \alpha_{Ii}(\omega,\hat{t}_{pi}) + \alpha_{Ij}(\omega,\hat{t}_{pj}) \qquad (A.16)$$

The $A(\hat{k},\omega)\ A(\hat{k}',\omega)$ term has dropped out since $\omega = -\omega'$ is not covered in the region of the integration. We have also defined a "retarded baseline":

$$\vec{B}_r \equiv \vec{x}_j(\hat{t}_{pj}) - \vec{x}_i(\hat{t}_{pi}) \qquad (A.17)$$

Let two particular parameters $(\beta,\ \gamma)$ define the direction vector. Suppose the brightness distribution is very narrow about some reference direction $\hat{k}_a$:

$$\hat{k}_a = \hat{k}\ (\beta_a,\ \gamma_a) \qquad (A.18)$$

If the brightness distribution is sufficiently compact, we can approximate the wave direction by

$$\hat{k} = \hat{k}_a + \left.\frac{\partial\hat{k}}{\partial\beta}\right|_a (\beta-\beta_a) + \left.\frac{\partial\hat{k}}{\partial\gamma}\right|_a (\gamma-\gamma_a) \qquad (A.19)$$

where the partials* are evaluated at the reference point β_a, γ_a. We then obtain

$$\langle v_i^q(\hat{t}_{bi})\ v_j^q(\hat{t}_{bj})\rangle = \frac{1}{2}\int_0^\infty R(u,v,\omega)\ G_i(\bar{\bar{y}}_i)\ G_j(\bar{\bar{y}}_j)\ e^{i\phi_f}\ d\omega + \text{c.c.} \qquad (A.20)$$

where

$$\bar{\bar{y}}_n = \omega\ (1 - \hat{k}_a \bullet \dot{\vec{x}}_n/c) \qquad n = i \text{ or } j \qquad (A.21)$$

$$\phi_f = \omega\ (\hat{t}_{pi} - \hat{t}_{pj}) + \vec{k}_a \bullet \vec{B}_r - \alpha_{Ii}(\omega,\hat{t}_{pi}) + \alpha_{Ij}(\omega,\hat{t}_{pj}) \qquad (A.22)$$

---

*Structure coordinates are usually defined as $\beta = (\alpha - \alpha_c)\cos\delta_c$ and $\gamma = \delta - \delta_c$ where $(\alpha_c,\ \delta_c)$ is the origin of structure coordinates relative to r.a. and declination. With this definition, the β partial and γ partial are in the direction of increasing right ascension and declination, respectively.

and where

$$R_B(u,v,\omega) \equiv \int_{-\infty}^{\infty}\int_{-\infty}^{\infty} S_p(\beta,\gamma,\omega)\, e^{-2\pi i[u(\beta-\beta_a) + v(\gamma-\gamma_a)]}\, d\beta d\gamma \tag{A.23}$$

for which

$$u \equiv - \left.\frac{\partial\hat{k}}{\partial\beta}\right|_a \bullet \frac{\vec{B}_r}{\lambda} \tag{A.24}$$

$$v \equiv - \left.\frac{\partial\hat{k}}{\partial\gamma}\right|_a \bullet \frac{\vec{B}_r}{\lambda} \tag{A.25}$$

$$\lambda = 2\pi c/\omega \tag{A.26}$$

With this definition, u and v are the components of the baseline vector projected on the plane of the sky.

Two approximations have been made in Eq. A.23. First, the weak $\hat{k}$ dependence in the bandpass functions has been neglected so that the y_i, y_j values have been evaluated at $\hat{k}_a$. Second, the limits of the (β, γ) integration have been extended to infinity under the assumption that the brightness distribution is very compact and terminates the integration. The function $R(u,v,\omega)$ is referred to as the brightness transform. A more detailed treatment of the brightness transform and of structure effects is given in Ref. 7.

The fringe visibility is the normalized modulus of the brightness transform and is a measure of the spatial extent of the source relative to the resolution of the interferometer for the given observation. It is equal to the ratio of "correlated flux" to total flux and is defined by

$$v_f(u,v,\omega) \equiv \left| \frac{R_B(u,v,\omega)}{R_B(0,0,\omega)} \right| \tag{A.27}$$

$$= \frac{\left| R_B(u,v,\omega) \right|}{S_p(\omega)} \tag{A.28}$$

where $S_p(\omega)$ is the total power emitted by all parts of the source at frequency ω. For a point source, the fringe visibility is unity for all baselines. For a diffuse source, the visibility is unity for a "null" baseline and decreases on the average as the baseline length increases. The decrease can become substantial for baselines satisfying

$$\left|\vec{B}_r\right| \gtrsim \frac{\lambda}{2d_s} \tag{A.29}$$

where d_s is the source diameter in radians and λ is the radio wavelength.

In addition to this normalization of the brightness transform, we must normalize the voltage signal in Eq. A.4. Using Eqs. A.10 and A.13 one can easily show that the expectation of the squared voltage is given by

$$\langle (v_n^q)^2 \rangle = \int_{\hat{k}} \int_0^\infty S_p(\hat{k},\omega)\; G_n^2(y_n)\; d\omega d\Omega \tag{A.30}$$

$$= \int_0^\infty S_p(\omega)\; G_n^2(\bar{\bar{y}}_n)\; d\omega \qquad n = i \text{ or } j \tag{A.31}$$

where we have again neglected the weak dependence of y_n on k and evaluated y_n at the reference position k_a. Using Eqs. A.6, A.17, A.20, A.22, A.28, and A.31, we can now compute the cross-correlation function for the normalized voltage components for the natural source:

$$\langle q_i(\hat{t}_{bi})\; q_j(\hat{t}_{bj})\rangle \equiv \frac{\langle v_i^q(t_{bi} - \tilde{\tau}_{mi} - \ell b)\; v_j^q(t_{bj} - \tilde{\tau}_{mj})\rangle}{\left[\langle (v_i^q)^2 \rangle \langle (v_j^q)^2 \rangle\right]^{1/2}} \tag{A.32}$$

$$= \frac{v_f}{2D_N} \int_0^\infty S_p(\omega)\; G_i(\bar{\bar{y}}_i)\; G_j(\bar{\bar{y}}_j)\; e^{i\phi_f}\; d\omega + \text{c.c.} \tag{A.33}$$

where

$$D_N^2 \equiv \int_0^\infty S_p(\omega)\; G_i^2(\bar{\bar{y}}_i)\; d\omega \int_0^\infty S_p(\omega)\; G_j^2(\bar{\bar{y}}_j)\; d\omega \tag{A.34}$$

and where

$$\begin{aligned}\phi_f = \phi_h - \omega_{hj}\,\tilde{\tau}_{mj} + \omega_{hi}(\tilde{\tau}_{mi} + \ell b) + \phi_I + \phi_B \\ + \vec{k}_a \cdot [\vec{x}_j(t_{pj} - \tilde{\tau}_{mj}) - \vec{x}_i(t_{pi} - \tilde{\tau}_{mi} - \ell b)] \\ + \omega(\tau_b + \tau_I + \tau_a - \tilde{\tau}_{mi} + \tilde{\tau}_{mj} - \ell b)\end{aligned} \tag{A.35}$$

in which τ_b, τ_I, τ_a, and ϕ_I are differences between station quantities in the order j minus i.

As explained in the text in Eq. 6.17, the timetag difference, $t_{pi} - t_{pj}$, is a combination of the difference in the errors in the bit times of the two stations and the difference in instrumental delays. We have pulled v_f out of the integral, recognizing that resolution of the source will vary very little across a 2-MHz passband located at RF. A phase term ϕ_B has been added to the fringe phase ϕ_f to represent the phase term from the brightness transform R. Further, we have used the definition of the instrumental phase from Eq. A.6, properly offset in time as indicated in Eqs. 6.8 and 6.9. Note that this expression for the fringe phase is the same as the expression (Eq. 6.13) assumed without proof in the text, except for the phase shift ϕ_e due to charged particles. The charged-particle phase shift has been added in an ad hoc fashion in the text to allow for such effects.

As indicated in Eqs. 6.5 and 6.7, the final expression (Eq. 6.10) for the cross-correlation function of an extended source is obtained by multiplying Eq. A.33 by $2/\pi$ and by a noise temperature factor. One can easily show that this result for an extended source is the same as that for a point source except that (a) an amplitude factor ($v_f < 1$) must be included, (b) a phase shift due to structure must be added to the phase, and (c) the wave direction is set equal to the reference direction $\hat{k}_a$.

APPENDIX B

THEORY FOR CALIBRATION-TONE PHASE

This appendix treats the subject of phase calibration with a tone generator and derives an expression for the stopped tone phase.

The calibrator signal, which consists of a sum of constant-frequency tones uniformly spread across the passband, is injected at a low power level near the front of the instrumentation and is imbedded in the radio source data. At the correlator, each tone is counter-rotated to nearly zero frequency by digitally mixing each single-station bitstream with a quadrature sinusoid whose frequency closely approximates the baseband frequency for that tone. After the resulting tone phase has been extracted and differenced between stations, it is subtracted from the interferometer (fringe) phase. Since the tones are subjected to the same instrumental effects as the natural source signal, instrumental effects between the injection point and the recorder cancel in the final difference. (This report will not consider difficulties encountered in calibration of instrumental effects before the injection point.)

Two types of phase calibrator are currently in use--the original Rogers version and the later Sigman version. The Rogers phase calibrator generates tones with a frequency spacing of 1 MHz. Its cable stabilizer records, but does not simultaneously remove, variations in the electrical length of the "uplink" cable. An average of the recorded variations is applied in subsequent processing to correct the composite observables obtained for an observation (e.g., over 3 minutes). With the Sigman calibrator, the frequency spacing of the tones can be set by the user to one of the values given by 5/N MHz, where N = 1, 2, ... or 99. The 5/N-MHz selection of zero crossings is automatically related to the station 1 pps signal in order to facilitate clock synchronization measurements. The Sigman calibrator continuously corrects for cable variations so that changes within an observation are automatically removed.

In this appendix, the tone phase is specified in terms of the various effects that enter the calibrator signal in transit from the clock through the instrumentation and then through data reduction. Since the analysis is based on an "ideal" model for the system, extra effort might be required to account for deviations from ideal behavior. It is beyond the scope of this report to assess all complications.

The model for the stopped tone phase is developed in the following sequence: (a) from the ϕ-cal clock to the injection point, (b) from the injection point to the recorder and (c) through the data reduction procedure. The simplified block diagram of the instrumentation shown in Fig. 6 will be useful in tracing the signal through the instrumentation.

First, for step (a), the phase of the signal at the clock reference point (ϕ-cal clock) discussed in Section IV and illustrated in Figure 6 is given in terms of true time and nominal frequency by

$$\phi_c = \omega_c \, (t + \tau_c) \tag{B.1}$$

as indicated by Eqs. 4.3 and 4.5. We have chosen to represent the calibration phase in this way since (a) the clock error τ_c is explicitly shown, (b) true time t is common to both stations, and (c) tone frequencies are calculated at the correlator on the basis of the nominal frequency ω_c. The signal will experience a cable delay τ_u so that its phase entering the tone generator will be given by

$$\phi_c = \omega_c \, (t + \tau_c - \tau_u) \tag{B.2}$$

The "ideal" tone generator converts the zero crossings of the "x-MHz" input signal (5 MHz for the Rogers version, 20 MHz for the Sigman version) into rectangular pulses as indicated schematically in Fig. 8. Repetition rates slower than x MHz are obtained by "eliminating" pulses. The passed repetition rate will be denoted by ω_p. As indicated below, the tone frequencies are the harmonics of the fundamental repetition rate ω_p.

In practice, there will be deviations from the ideal waveforms shown in Fig. 8, deviations such as delays, phase shifts and an amplitude distortion arising in both the tone generator and connecting elements. For example, a zero crossing is not precisely at the center of a rectangular pulse and the pulse shapes are not perfect rectangles. This report will not consider such deviations. (It should be pointed out that a constant deviation from rectangularity will cause clock synchronization measurements to be biased by a constant error that is less than the pulse width but will cause no error in geophysical/astrometric measurements.)

The output of the tone generator can be decomposed into its harmonics, which will have frequencies given by $n\omega_p$ (see Appendix F in [1]). The phase of the n^{th} calibration harmonic (tone) at the injection point will be given by

$$\phi_n^T = \omega_n^T \, (t + \tau_c - \tau_u) \tag{B.3}$$

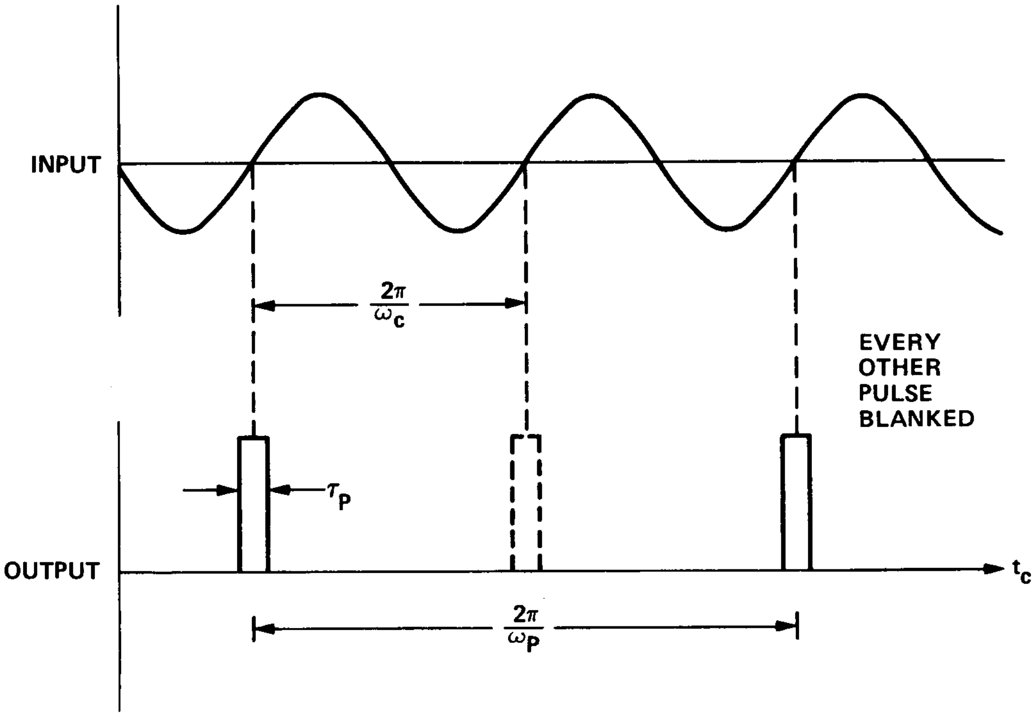

Figure 8. Input and Output Signals for the Ideal Tone Generator

The small group delays from the input of the tone generator to the injection point have not been explicitly represented since they (or any other group delay between the ϕ-cal clock and injection point) can be included in τ_u.

We are now prepared to model effects on the tone phase introduced in transit from the injection point to the recorder and then through the tone-stopping process. After injection, the tones, along with the natural source signal, pass through various filters and mixers until they reach baseband within a 2-MHz bandwidth. As in the case of the natural source signal (Eq. 5.5), the effects of these instrumental stages can be represented by lumped variables so that the phase of the n^{th} tone recorded at bit time t_{bk} for station k becomes

$$\phi^T_{nk}(t_{bk}) = \omega^T_n(t_{pk} + \tau_{ck} - \tau_{uk}) - \omega_{hk}\, t_{pk} - \phi_{hk} - \phi_{Ik}(\omega^T_n) \qquad \text{(B.4)}$$

$$k = i \text{ or } j$$

where t_{pk} is given by Eq. 5.6. Again, t_{pk} is the true time that corresponds to bit time t_{bk} at station k. Note that the delay τ_{ak} does not appear, since the phase-calibration signal is not subjected to antenna delays.

The recorded tones are processed at the same time the tapes are cross-correlated. The correlator uses a best estimate for the baseband frequency of each calibrator tone to separately "fringe-stop" each tone in a bitstream (see Appendix F in [1]). That is, in effect, the correlator will subtract from the phase of the n^{th} tone the phase

$$\psi^T_{nk} = (\omega^T_n - \hat{\omega}_{hk}) \quad (t_{bk} - t_s) \qquad \text{(B.5)}$$

which, based on Eq. 5.6, is also equal to

$$\psi^T_{nk} = (\omega^T_n - \hat{\omega}_{hk})\ (t_{pk} + \tau_{bk} + \tau_{Ik} - t_s) \qquad \text{(B.6)}$$

where $\hat{\omega}_{hk}$ is the best (nominal) estimate for the heterodyne frequency, t_{bk} is the bit time at station k, and t_s is the reference time adopted by the correlator. For phase calibration to work properly, it is necessary to use the same values for

$\hat{\omega}_{hk}$ and t_s in both the tone model phase (Eq. B.5) and the cross-correlation model phase (Eq. 7.1). The stopped-tone phase at station k becomes

$$\Delta\phi_k^T(\omega_n) = \phi_{nk}^T - \psi_{nk}^T \tag{B.7}$$

which, based on Eqs. B.4, B.5 and 5.6, is equal to

$$\Delta\phi_k^T(\omega_n) = -\ \omega_n^T\ (\tau_{bk} - \tau_{ck} + \tau_{uk} + \tau_{Ik} - t_s) \tag{B.8}$$

$$-\ \phi_{Ik}(\omega_n) - \Delta\phi_{hk}$$

where the "stopped" heterodyne phase is given by

$$\Delta\phi_{hk} = \omega_{hk}\ t_{pk} + \phi_{hk} - \hat{\omega}_{hk}\ (t_{bk} - t_s) \tag{B.9}$$

This puts the stopped-tone phase in the form we want, expressed in terms of contributing effects due to instrumentation and correlator processing. This analysis has neglected some subtle but important problems that can seriously degrade the stopped tone phase. These problems arise from unwanted intermodulation of frequency components in the calibrated signal with frequency components in the stopping function, where the resultant, possibly aliased, frequency of the intermodulation product happens to be close to the frequency of the stopped tone. Such problems have been greatly reduced in the BLKII processor by quantizing the counter-rotation tone sinusoids to 128 amplitude levels.

Another fact ignored to this point is that the measured tone phase, like the interferometer phase, has integer-cycle ambiguities. Ambiguity resolution for tones falls into two categories: relative and absolute. By relative ambiguity resolution we mean the removal of ambiguities in a relative sense between tones within a channel passband. If relative ambiguities are not removed, the variation of phase with frequency within a passband cannot be determined and correct interpolations in frequency cannot be made. To remove relative ambiguities, one must have an a priori estimate of the slope of phase vs. frequency, which means one must have estimates for terms multiplying ω_n in Eq. B.8. Those terms are the correlator reference time t_s, the calibrator cable delay (τ_u), the instrumental delay from the tone injection point to the recorder (τ_I), and the epoch offset ($\tau_b - \tau_c$) between the recorder clock and the ϕ-cal clock. The maximum allowed a priori error on these terms depends on tone spacing. For example, if the closest tones are separated by 1 MHz, then the collective a priori error (3σ) on these terms must be less than 0.5 microseconds.

After relative ambiguities have been removed, there will remain in the tone phases for each passband an overall integer-cycle ambiguity that is the same for all frequency points in the passband. That is, the tone phase will not be corrected for "absolute" integer cycles due to instrumentation. Accurate measurement and application of only the fractional part of the overall tone phase, however, adequately prepares the fringes for coherent addition over time and RF frequency and for an unambiguous estimate of BWS delay.

APPENDIX C

REFORMULATION OF THE FRINGE FITTING EQUATIONS

Insight into the least-squares fit to the fringes produced by Tensor can be enhanced by reformulating the output fringes under some simple assumptions. The reformulation leads, for example, to formulas for computing reference time t_z, reference frequency ω_z, and effective frequencies for charged-particle calibration.

First, rewrite the expression for the expectation value for the observed fringes in Eq. 13.7 in the form

$$\langle R(\tau_f,\omega_f) \rangle = S_c \sum_{k,n} c_{kn}\, e^{i\phi_{Rk}(t_n)} \tag{C.1}$$

where t_n is the n^{th} value for Greenwich time t_G and where the fringe phase for bin k at time t_n is given by

$$\phi_{Rk}(t_n) = \omega_k\, \Delta\tau_R(t_n) + \phi_B + \phi_e - (\omega_k - \omega_z)\tau_f - (t_n - t_z)\omega_f \tag{C.2}$$

and where c_{kn}, which is theoretically given by Eq. 11.2, is the true relative channel amplitude, scaled in the ideal case to set the overall amplitude equal to the correlated flux S_c. The subscript n has been added to c_k in order to explicitly denote the time dependence contained in $b_N(t_G)$. It has been assumed here that the correlated flux is constant across the spanned bandwidth.

The model fringes in Eq. 14.1 can be cast in the form

$$R_m(\tau_f,\omega_f) = A_s \sum_{k,n} c^m_{kn}\, e^{i\phi^m_{Rk}(t_n)} \tag{C.3}$$

where the model phase is given by

$$\phi^m_{Rk}(t_n) = (\omega_k - \omega_z)\ (\tau_s - \tau_f) + (t_n - t_z)\ (\omega_k\dot{\tau}_{\phi s} - \omega_f) + \phi_s \tag{C.4}$$

in which A_s, τ_s, $\dot{\tau}_{\phi s}$, and ϕ_s are the adjustable parameters. The form of the model amplitude c^m_{kn} depends on the approach used to normalize the fringes. The derivation of this appendix is valid for both approaches to normalization discussed in Section XI.

To determine how the fringe phase is implicitly fit with the model phase during estimation, consider a fit to the average fringes in which the sum

$$L_F \equiv \sum_{\tau_f, \omega_f} \left| \langle R(\tau_f, \omega_f) \rangle - R_m(\tau_f, \omega_f) \right|^2 \tag{C.5}$$

is minimized as a function of the four adjustable parameters. Completing the square, one obtains

$$L_F = \sum_{\tau_f, \omega_f} \left[|\langle R \rangle|^2 + |R_m|^2 - (\langle R \rangle R_m^* + c.c.) \right] \tag{C.6}$$

which can be rewritten as

$$\begin{aligned} L_F = \sum_{\tau_f, \omega_f} \sum_{k,k'} \sum_{n,n'} \Big[& S_c^2 \, c_{kn} \, c_{k'n'} \, e^{i(\phi_{Rk} - \phi'_{Rk'})} \\ & + A_s^2 \, c^m_{kn} \, c^m_{k'n'} \, e^{i(\phi^m_{Rk} - \phi^{m'}_{Rk'})} \\ & - (S_c \, A_s \, c_{kn} \, c^m_{k'n'} \, e^{i(\phi_{Rk} - \phi^{m'}_{Rk'})} + c.c.) \Big] \end{aligned} \tag{C.7}$$

The sum over τ_f, ω_f can now be carried out by interchanging the sum order, which results in sums of the form

$$S_\omega = \sum_{\omega_f} e^{i(t_n - t_{n'})\omega_f} \tag{C.8}$$

and

$$S_\tau = \sum_{\tau_f} e^{i(\omega_{k'} - \omega_k)\tau_f} \tag{C.9}$$

As mentioned in the text, the least-squares fit to the fringes will be applied to (τ_f, ω_f) points in the vicinity of the peak point. For an accurate model (e.g., accurate values for the relative amplitudes c^m_{kn} and fringes coherent over time and frequency as assumed in the model fringes in Eq. C.4), one would expect the parameter values estimated from a restricted set of points that include the bulk of the power in the peak area to be the same as the parameter values estimated from all points, on the average. (One can show that the partial derivatives of the fringes with respect to the estimated parameters reach maximum value in the vicinity of the peak so that the peak area dominates the solution.) Thus, for the purposes of this analysis, the fit region can be extended to cover all τ_f – ω_f points produced by Tensor. Given this complete range, the DFT phaser sums in Eqs. C.8 and C.9 are proportional to Kronecker delta functions:

$$S_\omega = \sum_{k=0}^{N_\omega - 1} e^{2\pi i(n-n')k/N_\omega} \propto \delta_{nn'} \tag{C.10}$$

and

$$S_\tau = \sum_{n=0}^{N_\tau - 1} e^{2\pi i(k-k')n/N_\tau} \propto \delta_{kk'} \tag{C.11}$$

The double sums over k and over n in Eq. C.7 each reduce to a single sum, which gives

$$L_F \propto \sum_{k,n} c^2_{kn} \left[S^2_c + A^2_s - 2S_c A_s \cos \Delta\psi_k(t_n) \right] \tag{C.12}$$

where it has been assumed that the model amplitude is very accurate ($c^m_{kn} = c_{kn}$) and where the residual phase is given by

$$\Delta\psi_{ck}(t_n) = \psi_c(\omega_k, t_n) - \psi^m_c(\omega_k, t_n) \tag{C.13}$$

in which the true phase is given by

$$\psi_c(\omega_k, t_n) = \omega_k \Delta\tau_R(t_n) + \phi_B(\omega_k, t_n) + \phi_e(\omega_k, t_n) \tag{C.14}$$

and the model phase by

$$\psi_c^m(\omega_k, t_n) = (\omega_k - \omega_z)\tau_s + (t_n - t_z)\omega_k \dot{\tau}_{\phi s} + \phi_s \tag{C.15}$$

If the model parameters are close to the final values and if the instrumentation is coherent in both time and frequency, the difference in the true phase and model phase will be a small fraction of a cycle for all values of k and t. Expanding the cosine under these assumptions, one obtains

$$L_F \propto (S_c - A_s)^2 \sum_{k,n} c_{kn}^2 + S_c A_s \sum_{k,n} c_{kn}^2 \, \Delta\psi_{ck}^2(t_n) \tag{C.16}$$

where terms higher than second order in differences have been discarded. (It should be noted that the phase nonlinearity over frequency introduced by the ionosphere will cause a small amount of incoherency across the spanned bandwidth. However, for current spanned bandwidths at S band (< 85 MHz at 2300 MHz) and at X band (< 400 MHz at 8400 MHz), the deviation from a linear phase model is sufficiently small to make this cosine expansion a good approximation, even for the worst-case ionosphere. For lower observing frequencies and/or larger fractional spanned bandwidths, the approximation should be reconsidered.) Thus, under the assumptions stated above, the least-squares fit of Eq. C.16 is, in effect, equivalent to two separate least-squares fits: one to the overall fringe amplitude (the first term in Eq. C.16) and one to the implicit phase values for each time and frequency point, with relative weights equal to c_{kn}^2 (the second term in Eq. C.16).

Given the least-squares form in Eq. C.16, one can readily show that the error in the output phase is decreased and that the correlation between the estimates for phase ϕ_s and for phase-delay rate $\dot{\tau}_{\phi s}$ is reduced if the reference time is given by

$$t_z = \frac{\sum_{k,n} c_{kn}^2 \, t_n}{\sum_{k,n} c_{kn}^2} \tag{C.17}$$

It has been assumed that the coefficients c_{kn} are nearly constant or factor (i.e., $c_{kn} = c_k' c_n''$). Similarly, the error in the output phase is decreased and the correlation between the estimates for BWS delay τ_s and phase ϕ_s is reduced if the reference frequency is given by

$$\omega_z = \frac{\sum\limits_{k,n} c_{kn}^2 \omega_k}{\sum\limits_{k,n} c_{kn}^2} \tag{C.18}$$

(After being calculated according to the last two formulas, these two reference values are imposed on the data through the counter-rotation in Eq. 13.6 and in the formation of the fringe fitting model in Eq. 14.1.) Given these definitions for t_z and ω_z and the above assumption concerning c_{kn}, one can easily show that the least-squares fit to phase in Eq. C.16 is equivalent to the following expressions for the estimated parameters:

$$\hat{\tau}_s = \frac{\langle(\omega - \omega_z)\psi_c\rangle_c}{\langle(\omega - \omega_z)^2\rangle_c} \tag{C.19}$$

$$\hat{\dot{\tau}}_{\phi s} = \frac{\langle(t - t_z)\omega\psi_c\rangle_c}{\langle(t - t_z)^2\omega^2\rangle_c} \tag{C.20}$$

$$\hat{\phi}_s = \langle\psi_c\rangle_c \tag{C.21}$$

where the averaging brackets are defined by

$$\langle f(\omega,t)\psi_c\rangle_c \equiv \frac{\sum\limits_{k,n} c_{kn}^2 f(\omega_k,t_n)\ \psi_c(\omega_k,t_n)}{\sum\limits_{k,n} c_{kn}^2} \tag{C.22}$$

and where ψ_c is given by Eq. C.14.

This analysis has provided formulas for computing the reference frequency and reference time used in data reduction and provided a method for computing how a given phase effect maps into the extracted observables. The validity of these equations, however, is dependent on the assumption that the model fringes in Eq. C.3 accurately represent the actual fringes. For that assumption to be valid, relative bin amplitudes must accurately model the actual relative bin amplitudes and the observed fringes must be sufficiently coherent over time and frequency. As indicated in the text, measures should be taken to insure the accuracy of the model.

APPENDIX D

DATA STRUCTURE IN THE TENSOR SOFTWARE

The data structure discussed in this appendix is specific to the current Tensor software. The discussion is limited to a high-level description, since it is outside the scope of this report to treat details of implementation and operation.

Fringes supplied to the Tensor software by the correlator are uniformly sampled in time but are sampled in RF frequency only within each 2-MHz channel. Sample spacing in time will be adjusted by the user according to the maximum residual fringe rate, while the frequency spacing will normally be 0.5 MHz between channel bins. For example, input points to the FFT along the frequency axis would number 800 for a 400-MHz spanned bandwidth, including the zero points used to fill the gaps between channels. However, the total number of points along the frequency axis will be 2048 after "rounding" 800 to the next highest value of 2**N (1024) and appending an array of 1024 zero points in order to double the sample rate in the output (BWS) delay variable. For this example, sample spacing along the output delay axis is $(0.5 \text{ MHz} \bullet 2048)^{-1} \approx 1$ nsec.

Figure 5a illustrates how the four bins from each of the 2-MHz channels are inserted in the 2048-point FFT buffer for a given integration interval of length T_a. These points are transformed by an FFT over frequency to the BWS-delay domain. After completion of the FFT for each time point, the output is saved for the subsequent FFT over time. Since the a priori delay uncertainty is usually much smaller than the span of delays covered in the FFT output, only a window of output points around the a priori delay value (at zero residual delay) is stored in the array memory, as illustrated in Figure 5a. For an a priori delay uncertainty of $\pm$250 nsec ($\pm$1 lag), only 512 of the 2048 output delay points are retained in this example. Note that for a standard FFT, the output points corresponding to negative delays are contained in the upper half of the FFT output and must be shifted to their proper position.

When all time points have been filled in, an FFT over time is performed on the fringes for each BWS delay. In analogy with the transform over frequency, the upper half of this array (in the time direction) can be filled with zeros in order to double the sample rate along the output fringe-frequency axis. The fringes produced by Tensor are a relatively complicated function of the delay and fringe frequency with a main lobe centered on the actual values for the delay and fringe frequency, as illustrated in Fig. 7. In the case of stable instrumentation and a low residual fringe rate, the functional form along the fringe frequency axis will be approximately equal to a sinx/x curve that peaks at the actual (residual) fringe frequency. Along the delay axis, the "delay resolution function" will peak at the actual (residual) delay if the channels have been made coherent by phase calibration. The sidelobe structure of the delay resolution function will depend on channel placement within the spanned bandwidth, the relative amplitudes of the channel fringes, and the coherence between channels.

APPENDIX E

ESTIMATION OF EFFECTIVE FREQUENCIES FOR CHARGED-PARTICLE CALIBRATION

The observables in Eqs. 14.6, 14.7, and 14.8 contain effective frequencies that must be specified in terms of channel-bin frequencies. This appendix derives approximate expressions for those effective frequencies and explains how they are used for charged-particle calibration.

The effect of charged particles on the fringe phase is given to good approximation at higher frequencies by

$$\phi_e(\omega) \approx \frac{k_e \; \Delta N_e(t)}{\omega} \tag{E.1}$$

where ω is the frequency, k_e is a constant, and ΔN_e is the difference in the integrated electron content along the two ray paths of the interferometer, in the order j minus i. The group delay corresponding to this phase shift is given by

$$\tau_e(\omega) = - \frac{\partial \phi_e}{\partial \omega} = \frac{k_e \; \Delta N_e}{\omega^2} \tag{E.2}$$

while the corresponding phase delay is given by the same expression but with opposite sign. The time derivative of the phase delay is also proportional to ω^{-2}. This ω^{-2} dependence can be utilized to essentially eliminate the ionosphere as an error source. If measurements of the group delay, phase delay, or phase-delay rate are made at two widely separated RF frequencies (ω_a, ω_b), then the observed values from the two RF bands can be combined as follows to eliminate the ionosphere delay (or delay rate):

$$O_{ab} = c_a O_a + c_b O_b \tag{E.3}$$

where O_a and O_b are the observed values and where

$$c_a = \frac{\omega_a^2}{\omega_a^2 - \omega_b^2} \tag{E.4}$$

$$c_b = -\frac{\omega_b^2}{\omega_a^2 - \omega_b^2} \tag{E.5}$$

If all other terms in the observables are non-dispersive (i.e., independent of frequency), those terms will "pass through" this calibration equation unchanged.

Since interferometry observables in a given band are often extracted from a wide bandwidth of frequencies (e.g., 400 MHz at 8400 MHz), it is not always obvious which frequency value (i.e., effective frequency) should be used for that band in Eqs. E.4 and E.5. This appendix derives formulas for estimating effective frequencies for the BWS delay, phase-delay rate and phase delay when these observables are extracted from a wide frequency band by the method outlined in Section XIV.

The importance of accurately estimating effective frequencies can be demonstrated by calculating the error in the calibrated delay that results from errors in those quantities. The delay values observed in two frequency bands are combined according to Eq. E.3 to obtain a corrected delay. If the errors in the estimates for the effective frequencies for the two bands are independent, one can readily show that the associated error in the calibrated delay is given by

$$\Delta\tau_\omega = \tau_e(\omega_b)\,\frac{2\omega_b^2}{\omega_b^2 - \omega_a^2}\left[\left(\frac{\Delta\omega_a}{\omega_a}\right)^2 + \left(\frac{\Delta\omega_b}{\omega_b}\right)^2\right]^{1/2} \tag{E.6}$$

where τ_e is the charged-particle delay at frequency ω_b and where $\Delta\omega_a$, $\Delta\omega_b$ are the errors in the effective frequencies. This expression can be used to derive a worst-case bound on the allowed errors in the effective frequencies. Suppose a) the maximum allowed delay error due to this effect must be less than 0.1 cm, b) the observing frequencies are S-band (2.3 GHz) and X-band (8.4 GHz), c) the 0.1-cm error budget is equally divided between the two bands, and d) the worst-case charged-particle delay is 200 cm at X-band (i.e., the maximum ionosphere at 0 deg elevation over the last few years). Under these assumptions, the maximum allowed errors in the effective frequency are 0.35 MHz at S-band and 1.4 MHz at X-band. Since the spanned bandwidth can currently be as large as 85 MHz at S-band and 400 MHz at X-band, these relatively tight constraints indicate that the effective frequencies should be determined with fairly good accuracy relative to the spanned bandwidth.

Approximate expressions for effective frequencies to be used in dual-band calibration can be derived as follows for the three types of observables. Eqs. C.19, C.20, and C.21 in Appendix C can be used to determine how a given phase effect maps into each of the three estimated parameters. For example, by substituting the expression in Eq. E.1 in place of ψ in Eq. C.19, one can determine the average change in estimated BWS delay due to charged particles:

$$\bar{\tau}_e = - \frac{\sum_{k,n} c_{kn}^2 \frac{k_e \Delta N_e(t_k)}{\omega_k} (\omega_k - \omega_z)}{\sum_{k,n} c_{kn}^2 (\omega_k - \omega_z)^2} \tag{E.7}$$

where a minus sign has been included to correspond with the convention in Eq. E.2.

To reduce this expression to a useful form, one must separately consider each normalization option discussed in Section XII. When no normalization is applied, Eq. E.7 is difficult to evaluate in the general case due to the possibility of time variation of b_n in the coefficients c_{kn}^2 (see Eq. 11.2). Thus, the simplifying assumption will be made that all time intervals for a given frequency channel have the same bit count, which leads to relative amplitudes that are independent of time (i.e., of n). The relative amplitudes are still given by Eq. 11.3 but with the understanding that N_t in Eq. 11.3 might change from channel to channel but is the same for all time points for a given channel. The charged-particle delay in Eq. E.7 can now be rewritten in the form

$$\bar{\tau}_e = \frac{k_e \, \Delta\bar{N}_e}{\omega_\tau^2} \tag{E.8}$$

where the effective frequency is defined by

$$\omega_\tau^2 \equiv - \frac{\sum_k c_k^2 (\omega_k - \omega_z)^2}{\sum_k c_k^2 \frac{(\omega_k - \omega_z)}{\omega_k}} \tag{E.9}$$

in which c_k is given by Eq. 11.2 with the appropriate value for b_n from Eq. 11.3 or 11.4. The quantity $\Delta\bar{N}_e$ denotes an unweighted time average across the observation.

In practice, actual bit counts will not necessarily conform to the aforementioned "stable-channel" assumption. Given a reasonably well-functioning system, however, this expression can still be used to obtain an accurate estimate of effective frequency if N_t in Eq. 11.3 is replaced by $\overline{N_k}$, the average of the bit counts for channel k across the observation.

In an analogous fashion, one can use Eqs. C.20 and C.21 to compute the average ionosphere effect in delay rate:

$$\overline{\dot{\tau}}_e = \frac{k_e \, \overline{\Delta \dot{N}_e}}{\omega^2_{\dot{\tau}}} \tag{E.10}$$

and in phase:

$$\overline{\phi}_e = \frac{k_e \, \overline{\Delta N}_e}{\omega_\phi} \tag{E.11}$$

where the effective frequencies are given by

$$\omega^2_{\dot{\tau}} \equiv \frac{\sum_k c_k^2 \, \omega_k^2}{\sum_k c_k^2} \tag{E.12}$$

and

$$\omega_\phi^{-1} \equiv \frac{\sum_k c_k^2 \frac{1}{\omega_k}}{\sum_k c_k^2} \tag{E.13}$$

Since phase-delay is obtained by dividing the phase by the reference frequency (see Eq. 14.8), the corresponding effective frequency for phase-delay becomes

$$\omega^2_{\tau\phi} = \omega_z \, \omega_\phi \tag{E.14}$$

where ω_z is the reference frequency defined by Eq. C.18. In Eq. E.10 the "average rate of change" of electron content is defined by

$$\overline{\Delta \dot{N}_e} = \frac{\sum_n (t_n - t_z)\Delta N_e(t_n)}{\sum_n (t_n - t_z)^2} \tag{E.15}$$

One can readily show that this weighted average is equal to $\Delta \dot{N}_e$ if the electron content increases linearly over time.

As an example calculation of effective frequencies, let the channel frequencies be given by

S-band = 2000 + (0, 45, 60, 75, 80, 85) MHz

X-band = 8000 + (0, 10, 40, 120, 210, 290, 340, 360) MHz

Note that, for simplicity, bin frequencies within each channel are not specified. This simplification will not affect the substance of this example. Given these channel frequencies and equal channel amplitudes c_{kn}, Table E-1 presents the effective frequencies predicted by Eqs. E.9, E.12 and E.14.

An unweighted average of the channel frequencies has been included in the table for comparison. Note that there is a 16-MHz spread in the S-band values even though the spanned bandwidth is only 85 MHz. A comparison of the spreads in these values with the worst-case accuracy requirements computed above (i.e., 0.35 MHz for S-band and 1.4 MHz for X-band) suggests that care must be taken in the computation of effective frequencies, particularly at S-band.

Table E-1. An Example of Effective Frequencies

Type	S-band	X-band
BWS delay	2041.76	8174.96
Phase delay	2057.29	8170.07
Delay rate	2057.70	8172.43
Average (ω_z)	2057.50	8171.25

The results of this appendix depend on an assumption made in the derivation of Appendix C, namely that the model fringes accurately represent the actual fringes. If this assumption is not satisfied, the preceding expressions for calculating the effective frequencies may not be sufficiently accurate. As indicated in the text, measures should be taken to insure the accuracy of the model.

TECHNICAL REPORT STANDARD TITLE PAGE

1. Report No. 87-29	2. Government Accession No.	3. Recipient's Catalog No.
4. Title and Subtitle Interferometry Theory for the Block II Processor		5. Report Date October 15, 1987
		6. Performing Organization Code
7. Author(s) J. B. Thomas		8. Performing Organization Report No.
9. Performing Organization Name and Address JET PROPULSION LABORATORY California Institute of Technology 4800 Oak Grove Drive Pasadena, California 91109		10. Work Unit No.
		11. Contract or Grant No. NAS7-918
		13. Type of Report and Period Covered External Report JPL Publication
12. Sponsoring Agency Name and Address NATIONAL AERONAUTICS AND SPACE ADMINISTRATION Washington, D.C. 20546		14. Sponsoring Agency Code RE211 BG-314-40-22-12-05

15. Supplementary Notes

16. Abstract

This report presents interferometry theory for the Block II processor, including a high-level functional description and a discussion of data structure. The analysis covers the major processing steps: cross-correlation, fringe counter-rotation, transformation to the frequency domain, phase calibration, bandwidth synthesis, and extraction of the observables of amplitude, phase, phase rate, and delay. Also included are analyses for fractional bitshift correction, station clock error, ionosphere correction, and effective frequencies for the observables.

17. Key Words (Selected by Author(s))	18. Distribution Statement
Electronics and Electrical Engineering; Space Sciences (General); Astronomy	Unclassified; unlimited

19. Security Classif. (of this report)	20. Security Classif. (of this page)	21. No. of Pages	22. Price
Unclassified	Unclassified		

JPL 0184 R 9/83